Late Neogene tectonically driven crustal exhumation of the Sikkim Himalaya: Insights from inversion of multithermochronologic data

Kyle R. Landry, Department of Earth Sciences, Dalhousie University, P.O. BOX 15000 Halifax, NS, B3H 4R2, CANADA

Isabelle Coutand, Department of Earth Sciences, Dalhousie University, P.O. BOX 15000 Halifax, NS, B3H 4R2, CANADA, icoutand@da.ca

David M. Whipp Jr., Institute of Seismology, Department of Geosciences and Geography, P.O. Box 68 (Gustaf Hällströmin katu 2b), FI-00014 University of Helsinki, FINLAND

Djordje Grujic, Department of Earth Sciences, Dalhousie University, P.O. BOX 15000 Halifax, NS, B3H 4R2, CANADA

Jeremy K. Hourigan, Department of Earth and Planetary Sciences, University of California Santa Cruz, 1156 High Street, Santa Cruz, CA 95064, USA

This article has been accepted for publication and undergone full peer review but has not been through the copyediting, typesetting, pagination and proofreading process which may lead to differences between this version and the Version of Record. Please cite this article as doi: 10.1002/2015TC004102

Abstract

Apatite fission-track, and zircon (U-Th)/He data are reported for 34 bedrock samples distributed between the foothills and the topographic crest of the Darjeeling-Sikkim Himalaya. The pattern of observed cooling ages do not correlate with topography, rainfall distribution and the deeply incised high-relief Tista window, indicating that tectonic processes are mainly responsible for their spatial distribution. Inversion of this thermochronometric dataset using 3D-thermokinematic modeling constrained by independent geological and geophysical observations was performed to evaluate the contribution of slip partitioning, duplex development and relief growth on the evolution of the thermal structure of the Himalaya during the last 12 Ma. Models involving significant relief growth do not show a substantial influence of topography evolution on the cooling age distribution while models involving duplex growth demonstrate that tectonic processes exert a dominant influence on their distribution. In concert with equivalent studies in Bhutan, central Nepal, and NW India, our results attest that the lateral variation of the geometry and kinematics of the Himalayan basal décollement exert a leading influence on lateral variations of mid- to upper crustal long-term exhumation rates documented along the strike of the Himalaya.

1. Introduction

Upper crustal exhumation in mountain ranges is intrinsically controlled by tectonic processes accreting material to the orogenic wedge and tectonically- or climatically-induced surface processes removing it out of the system through erosion and transport [e.g. *Whipple*, 2014; *Whipple*, 2009]. Relationships between orogenic erosion and climatic cycles in glaciated landscapes have been extracted from low-temperature thermochronometric datasets at various spatial scales [e.g. *Herman et al*., 2013; *Shuster et al*., 2005; *Thomson et al*., 2010]. This exercise, however, proves being more challenging in fluvial landscapes where interpretations of thermochronometric datasets fail to unambiguously establish causal relationships between short-term climatic variations (rainfall distribution) and changes in long-term erosion rates [e.g. *Thiede and Ehlers*, 2013 and references therein]. Instead in the Himalaya, there are numerous lines of evidences that structural variation along the strike of the orogen account for most of the characteristics and variations of low-temperature thermochronometric datasets [*Adlakha et al*., 2013; *Célérier et al*., 2009; *Coutand et al*., 2014; *Herman et al*., 2010; *McQuarrie and Ehlers*, 2015; *Robert et al*., 2011; *Thiede and Ehlers*, 2013; *Whipp et al*., 2007]. Yet there is no consensual tectonic model for the late Neogene (post-10 Ma) tectonomorphic evolution of the range, probably owing to the structural variability along the Himalayan arc and the applicability of different tectonic models in different locations. Three main groups of tectonic models have been proposed to explain the development of the frontal part of the Himalaya during the last 10 Ma (see Figure 3 in *Herman et al*., 2010). The first group involves the overthrusting of the orogenic wedge along a crustal-scale basal décollement with laterally changing geometry and kinematics [e.g. *Coutand et al*., 2014; *Gansser*, 1964; *Robert et al*., 2009; *Robert et al*., 2011]. The second group implicates the growth of duplexes at mid- [e.g. *Avouac*, 2003; *Bollinger et al*., 2004; *Bollinger et al*., 2006; *Herman et al*., 2010] to upper-crustal depths [e.g. *DeCelles et al*.,

1998; *Long et al*., 2011a; *Bhattacharyya and Mitra*, 2009; *McQuarrie and Ehlers*, 2015; *Robinson and Martin*, 2014] as a result of horizontal shortening and localized crustal accretion. The third group involves out-of-sequence thrusting where the MCT, whose ductile activity mostly ceased by the end of the Middle Miocene, is reactivated in the late Miocene-Pliocene [*Catlos et al*., 2001; *Harrison et al*., 1997] to Plio-Pleistocene [*Hodges et al*., 2004; *Mukul*, 2000; *Wobus et al*., 2005] in response to climatically focused erosion.

Inversion of thermochronometric datasets using thermokinematic modeling constrained by independent geological observations is a useful approach to help discriminate between these three groups of models, because the kinematics and geometry of the major structures across orogens, combined with changing topography, may strongly affect the thermal structure of the middle and upper crust [e.g. *Braun*, 2005; *Ehlers*, 2005; *Mancktelow and Grasemann*, 1997; *Stüwe et al*., 1994; *Whipp et al*., 2007]. In this study, we use a modified version of the 3D-thermokinematic model *Pecube* [*Braun*, 2003; *Braun et al*., 2012] to invert a new set of 15 zircon (U-Th)/He (ZHe), 19 apatite fission track (AFT) data and five published AFT ages [*Kellett et al*., 2013] located along a North-South oriented transect across the Sikkim Himalaya (Figure 1) to identify the mechanisms that have contributed to the late Neogene tectonomorphic development of this part of the Himalayan orogen.

2. Geological setting

Since collision occurred ~ 55-60 Ma ago [*Najman et al*., 2010; *Zhuang et al*., 2015], the ongoing convergence between India and Eurasia formed the Himalayan orogen, which is characterized by four lithotectonic units bounded by north-dipping crustal-scale shear zones or thrust faults that are continuous across the 2500 km length of the orogen (for reviews, see *Hodges*, 2000; *Yin*, 2006). From north to south, these units are (Figure 1) the Tethyan Sedimentary Sequence (TSS), the amphibolite to granulite metamorphic grade rocks and Miocene leucogranites of the Greater Himalayan Sequence (GHS), the metasediments of the

Lesser Himalaya Sequence (LHS), and the Miocene-Pliocene synorogenic foreland sediments, which are thrust over the Ganges-Brahmaputra foreland basin along the active Main Frontal Thrust (MFT). Major shear zones include the ~23-13 Ma coevally active South Tibetan Detachment System (STDS) and Main Central Thrust (MCT) [*Godin et al*., 2006], the > 10 Ma Main Boundary Thrust (MBT) [*Meigs et al*., 1995] and the < 2 Ma Main Frontal Thrust (MFT) [*van der Beek et al*., 2006]. These faults branch at depth from a major shear zone, the Main Himalayan Thrust (MHT) [*Acton et al*., 2011; *Alsdorf et al*., 1998; *Nábělek et al*., 2009; *Nelson et al*., 1996] along which the Indian crust is underthrusted beneath the southern portion of Tibet. The Sikkim Himalaya is located in a transition zone between Nepal to the west and Bhutan to the east, which have different structural, climatic and geomorphological characteristics. The main differences are: 1) klippen of TSS metasediments preserved atop the GHS in Bhutan while Sikkim and Nepal are marked by proportionally larger exposure of LHS unit in pervasive tectonic windows (Figure 1 in *Coutand et al*., 2014) suggesting greater exhumation in the west, 2) different topographic profiles with two-step morphologies in central Nepal and Sikkim and a nearly straight taper rising from the foreland in Bhutan [*Duncan et al*., 2003] controlling the various extent of precipitations penetrating into the orogen [*Bookhagen and Burbank*, 2010], 3) the presence of the Shillong plateau south of Bhutan, a 1600 m-high orographic barrier uplifted during the Pliocene [*Biswas et al*., 2007; *Najman et al*., 2016] causing tectonic and possibly climatic perturbations in eastern Bhutan, [*Biswas et al*., 2007; *Clark and Bilham*, 2008] that do not affect Sikkim and Nepal. Finally, the Yadong Graben is a transverse structure that also might have contributed to the morpho-tectonic differences observed between Bhutan and Sikkim. In the following section, we review the main geophysical, geological, structural and geochronological aspects of Sikkim geology relevant to determine the parameter ranges used to constrain our thermokinematic models.

2.1. The Tethyan Sedimentary Sequence and the South Tibetan Detachment system

The Tethyan Sedimentary Sequence (TSS) is a continuous unit extending from northern Sikkim to the Indus-Yarlung suture zone (Figure 1) and composed of un-metamorphosed to greenschist facies Devonian to Jurassic marine shales and carbonates, associated with continental sandstones and conglomerates [*Gaetani and Garzanti*, 1991; *Garzanti*, 1999]. The TSS is bounded to the south by the South Tibetan Detachment system (STDS) [*Burchfiel and Royden*, 1985; *Burg et al*., 1984; *Kellett and Grujic*, 2012; *Kellett et al*., 2013] a northward shallow-dipping normal-sense shear zone which in Sikkim, is cut by a steeper north-dipping network of minor brittle normal faults [*Kellett et al*., 2013] and by seismically active north-south striking normal faults apparently synthetic to major structures forming the Yadong Graben [*Pradhan et al*., 2013]. Ductile deformation initiated at ~23 Ma as determined by U-Th-Pb dating of prograde monazites within garnets, and by Lu-Hf dating of garnets from the highly sheared garnet granite–gneiss [*Anczkiewicz et al*., 2014], and ceases by ~14 Ma, as documented by zircon U-Pb dating of cross cutting and little deformed leucogranites [*Kellett et al*., 2013]. Muscovite $^{40}Ar/^{39}Ar$ (MAr), AFT and apatite (U-Th)/He (AHe) data from the immediate footwall of the STD shear zone yield near identical ages of 13-14 Ma, and together with higher temperature geochronological data, are interpreted as recording transient rapid cooling and the end of displacement on the STDS in Sikkim [*Kellett et al*., 2013].

2.2. The Greater Himalayan Sequence and the Main Central Thrust zone

In Sikkim, the Greater Himalayan Sequence (GHS), also refereed to as the Darjeeling formation [*Acharyya and Ray*, 1977] or the Higher Himalayan Crystalline Complex [*Neogi et al*., 1998], is a suite of amphibolite to granulite facies metamorphic rocks [*Chakraborty et al*., 2003; *Dasgupta et al*., 2004; *Ganguly et al*., 2000; *Harris et al*., 2004; *Rubatto et al*., 2013] exposed between the STDS in the north and the MCT in the south (Figure 1), which was

intruded by leucogranites emplaced between 23-12 Ma [*Kellett et al*., 2013; *Rubatto et al*., 2013].

In Sikkim, the MCT corresponds to a zone up to 10-20 km wide (in map view, Figure 1) of penetrative ductile shear associated with an inverted metamorphic sequence [*Dasgupta et al*., 2004; *Harris et al*., 2004; *Mohan et al*., 1989; *Mottram et al*., 2014b; *Neogi et al*., 1998; *Anczkiewicz et al*., 2014; *Gaidies et al*., 2015; *von Loczy*, 1907]. It has been suggested that the shear zone is bounded by two north-dipping thrusts variably named MCT_1 and MCT [*Catlos et al*., 2004], MCT_2 and MCT_1 [*Bhattacharyya and Mitra*, 2009; 2011] or MCT and HHT (High Himalayan Thrust, *Grujic et al*., 2011). Otherwise, the MCT has been placed at the top or at the bottom of the MCT shear zone (see *Mottram et al*., 2014a and references therein). In this study, we use the location of the MCT as defined by *Mottram et al*., (2014a) and following *Davidson et al*., (1997), consider it as a protolith boundary between the GHS- and LHS-derived mylonites, located within a wide ductile shear zone (Figure 1). The ductile movement in the MCT shear zone lasted between 20-23 and 12-10 Ma as documented by Th-Pb ages on monazite [*Catlos et al*., 2004; *Mottram*, 2014; *Mottram et al*., 2014a] and Sm-Nd [*Harris et al*., 2004] and Lu-Hf ages on garnet [*Anczkiewicz et al*., 2014]. The development of duplex structures in the underlying LHS [*Bhattacharyya and Mitra*, 2009] has folded the MCT (Figure 2) and in concert with the localized fluvial incision of the GHS nappe by the Rangit and Tista rivers, has exposed the underlying LHS in the Tista half window (Figures 1 & 2).

2.3. The Lesser Himalayan Sequence and the Lesser Himalayan Duplex

The Lesser Himalayan Sequence (LHS) exposed in Sikkim consists of three units: The Daling group, the Baxa and the Gondwana Formations [*Bhattacharyya and Mitra*, 2009; *Schwan*, 1980] (Figures 1 & 2). The Mesoproterozoic Daling Group is divided into the quartzitic Reyang Formation overlain by the meta-pelitic Daling Formation and is suggested

to have a maximum thickness of ca. 5 km [*Bhattacharyya and Mitra*, 2009]. The Baxa Fm. interpreted to be Late Neoproterozoic in age [*Schopf et al*., 2008 and references therein] is composed of both marine and continental carbonaceous slates and interbedded quartzites, limestones and conglomerates up to 1.2 km thick [*Bhattacharyya and Mitra*, 2009]. At the top of the sequence, the Gondwana Formation lies unconformably on the Baxa Formation and is an up to 1 km thick section of basal conglomerates overlain by arkoses, quartzites and topped by carbonaceous slates [*Bhattacharyya and Mitra*, 2009]. Various plant fossils found within this unit suggest a Permian depositional age in a subaerial environment [*Acharyya*, 1971].

The LHS rocks have been shortened and stacked to form a prominent and composite structure made of two imbricated duplexes and referred to as the Lesser Himalayan Duplex (LHD) in Figure 2. It is composed of the Rangit duplex incorporating the Daling, Baxa and Gondwana units, with the MBT forming the floor thrust and the Ramgarh Thrust (RT) forming the roof thrust (Figure 2). Rangit duplex is structurally overlain by the Daling duplex, which has the MCT as a roof thrust [*Bhattacharyya and Mitra*, 2009; *Mitra et al*., 2010; *Mukul*, 2010] (Figures 1 & 2). The age and structure of the inverted Barrovian sequence within the Daling duplex indicates that it has developed together with the formation of the MCT zone [*Anczkiewicz et al*., 2014; *Mottram et al*., 2014a]. Bouguer anomaly modeling suggests a total thickness of up to 12 km of the stacked LHS units in central Sikkim [*Tiwari et al*., 2006]. The frontal (southern) horses of the Rangit duplex form a foreland-dipping structure, the middle part form an antiformal stack and the rear (northern) part are hinterland-dipping horses [*Bhattacharyya and Mitra*, 2009; *Mitra et al*., 2010]. South of the LHD, erosional remnants indicate that the GHS nappe used to extend well south of Darjeeling (Figures 1 and 2). The growth of the Rangit duplex has folded the overlying Daling duplex and the GHS into open upright NS and EW trending antiforms, that have

subsequently been incised by the Tista and Rangit rivers resulting in the exposure of underlying LHS terranes in the double tectonic window (Figure 1). Hence, the Rangit duplex must have formed after cessation of the MCT activity 12-10 Ma ago.

2.4 The Main Boundary Thrust, the Siwaliks Group and the Main Frontal Thrust

The LHS is bounded to the south by the Main Boundary Thrust (MBT), a thrust fault steeply dipping (~50°) towards the NNE [*Mukul*, 2000] that carries the Gondwanan metasediments on top of the lower Siwaliks foreland basin deposits (Figures 1 & 2). There is no direct dating of this structure's activity, but it is reasonable to assume that it might have become active to accommodate ongoing India-Eurasia convergence when displacement on the MCT ceased 12-10 Ma ago, in concert with the development of the Rangit duplex. The MBT seems to be locally folded by the activation of the South Kalijhora Thrust, a new fault formed in its footwall during the Quaternary [*Mukul*, 2000; *Kellett et al*., 2014].

In the footwall of the MBT, an imbricate zone associated with uplifted fluvial strath terraces repeats the Siwalik Group multiple times and indicates neotectonic activity in the frontal part of the wedge [*Mukul*, 2000; *Mukul et al*., 2007]. The southern boundary of the Siwaliks is the Main Frontal Thrust (MFT), the southernmost thrust fault in the Himalayan orogenic wedge and the active toe of the Himalaya [*Lavé and Avouac*, 2000]. In West Bengal, the MFT is rarely exposed at the surface (Figure 1) and carries the Siwalik Group atop of the modern foreland basin. Combined optically and thermally stimulated luminescence dating of fault gouge from the MFT yielded ages of ~ 40 ka showing it was active until at least the late Pleistocene [*Mukul et al*., 2007].

2.5. Constraints on the Main Himalayan Thrust geometry

In Sikkim, constraints on the geometry of the basal décollement, the Main Himalayan Thrust (MHT), are based on geophysical data and balanced cross-sections (Figure 2). In the southern part of the section at ca. 88.20°E, the MHT is suggested to dip northwards at ~ 4°

(average slope distributed over 3 flats and ramps segments) at a depth between 8 and 12 km beneath the Tista-Rangit double window [*Bhattacharyya and Mitra*, 2009; *Mitra et al*., 2010] (Figures 1 and 2). Projected receiver function data [*Acton et al*., 2011] suggest that the MHT lies at a depth of 10-15 km between 30 to 80 km north of the surface trace of the MBT, where it starts to dip northward at 15-20º, connecting at about 27.75°N with the MHT imaged at a depth of ~ 30-35 km on INDEPTH profile Tib-1 [*Hauck et al*., 1998].

3. Thermochronologic data

3.1. Data collection

We present a dataset of 34 new ages and 5 published ages from [*Kellett et al*., 2013], comprising two different low-temperature thermochronologic systems: apatite fission-track (AFT), and zircon (U-Th)/He (ZHe). These thermochronometers were selected due to their ability to record cooling and exhumation through the upper 5 to 7 km of the crust. Typical effective closure temperatures are 120 ± 20 °C (AFT) [*Donelick et al*., 2005], and 170 ± 20 °C (ZHe) [*Reiners*, 2005], though the closure temperatures vary with chemical composition of the crystals, concentration of alpha radiation damage, grain size and cooling rate among other factors. Analytical techniques used for data acquisition are reported in the Supporting Information (S1 and S2).

Samples were collected along north to north-northeast oriented transects (Table 1, Figure 1) starting in the hanging-wall of the MBT at Kalijhora, and continuing northwards across the Gondwana Formation and the LHS at Kalimpong. There, the line of samples splits into two routes: One across western Sikkim traversing the Tista and Rangit windows, the MCT and the GHS to finish at Goecha La in the Kanchenjunga National Park, and a second across eastern Sikkim through Gangtok within the LHS, across the MCT shear zone to remain in the GHS from Chungthang up to the footwall of the STDS in the north (Figure 1).

3.2. Results

3.2.1. Apatite fission-track thermochronology

Out of 32 samples processed for AFT thermochronology, about one-third had apatite yields of poor quality due to low U concentrations, U zoning, cracks, inclusions or even absence of crystals, and only 19 samples have provided reliable results (Table 2). The samples were processed at the Dalhousie Fission-Track Laboratory (for analytical procedure, see S1). Between 12 and 20 grains were dated per sample, and all the samples passed the χ^2 test indicating that the single-grain ages are consistent with a common age for each sample. AFT cooling ages are mostly Plio-Pleistocene and range between 0.6 ± 0.1 Ma and 5.6 ± 0.5 Ma (Table 2). These young ages indicate fast cooling and, together with low-uranium concentrations, did not allow measurement of confined tracks.

3.2.2. Zircon (U-Th)/He thermochronology

Fifteen samples were processed for ZHe dating at both the Dalhousie Noble Gas Extraction Laboratory and the Keck Isotope Laboratory at the University of California Santa Cruz (for analytical procedure, see S2). For each sample, five acceptable grains were selected for dating, except for samples ISIK36 and ISIK42 in which only three and four suitable grains were found (Table 3). A total of 72 zircon aliquots were processed in this study. Six samples yielded well-reproducible single-grain ages for the five aliquots, six samples for four aliquots, two samples for three aliquots and one sample for two (sample ISIK36) (Table 3). Some aliquots were discarded on the basis of anomalous isotopic values (for example, ISIK42-5 and ISIK 38-4 yielded low to undetectable ^{4}He quantity), and others because they yielded outlier ages defined as being more than 50% older or younger than the rest of the grains in their respective samples. ZHe cooling ages are Late Miocene-Pleistocene and range between 11.87 ± 0.49 Ma and 1.30 ± 0.07 Ma (Table 3).

3.3. Age patterns along the transect

In order to describe the distribution of cooling ages across the study area, each sample location was projected perpendicularly onto cross-section line BB' (Figure 1) and plotted against latitude, or distance along section (Figure 3). The dataset shows a symmetrical concave-upward pattern with the oldest ages located immediately north of the MBT (~ 12 Ma for ZHe and 5-6 Ma for AFT), an abrupt decrease between 27.1 and 27.75°N (~ 1-3 Ma for ZHe and 0.5-1.5 Ma for AFT), and a rapid increase of AFT ages 12.5 Ma in the footwall of the STDS. Importantly, (1) this age-trend is apparently not perturbed across the MCT, suggesting that the activity of the shear zone ended by the time of cooling of the samples through their respective closure temperatures, (2) the age values do not correlate with sample elevations (Figure S3 in Supplementary Material) and modern rainfall distribution (Figure 3), and (3) the Tista window contains a wide array of ages (instead of concentrating only young ages), suggesting that river incision that carved these windows may not be the dominant process responsible for the cooling age distribution.

4. Thermo-kinematic modeling

The new thermochronologic dataset is combined with existing data from *Kellett et al*., [2013] (Figure 1, Table 1) to perform a formal inversion and assess the sensitivity of the cooling age distribution to localized enhanced rock uplift (simulating duplex formation) and river incision. The inversion uses the Neighbourhood Algorithm software (*Rickwood and Sambridge*, 2006; *Sambridge*, 1999a; b) to select input values for three-dimensional (3D) thermo-kinematic models (*Pecube*; *Braun*, 2003) and determine the ranges of relevant geological parameters such as fault slip rates, fault geometry, the location and rates of localized crustal accretion, potential changes in topography, and the thermal properties of the surrounding crust. A complete description of the inversion procedure can be found in

Coutand et al. [2014] and references therein. Below we describe key features and differences from the approach used by *Coutand et al*. [2014].

4.1. Forward model Pecube and model input parameters (Table 4)

Thermochronometer cooling ages are predicted for comparison with observed ages by forward modeling the 3D crustal thermal field using a modified version of the software *Pecube* [*Braun*, 2003; *Braun et al*., 2012]. In the model, mass transport is calculated using the combination of a simple fault with variable geometries and slip rates, and localized zones of enhanced rock uplift simulating duplex formation. The resulting velocity field defines the exhumation pathways of points coincident with sample locations in the model and their cooling histories during exhumation. The thermochronometer-specific age prediction algorithms use the resulting cooling histories to predict cooling ages that are compared to the observed age data.

Model temperatures are calculated using an iterative solution to the finite-element formulation of the 3D thermal advection-diffusion equation [*Braun et al*., 2012],

$$\rho c\left(\frac{\partial T}{\partial t} + v\nabla T\right) = k\nabla^2 T + H, \quad (1)$$

where ρ is density, c is heat capacity, T is temperature, t is time, v is the velocity field, k is thermal conductivity and H is volumetric radiogenic heat production (for units and symbols, see Table 4). A steady-state thermal solution is found at the start of the simulation at 12 Ma, using the fault geometry and topography in the model at that time. The transient thermal field is calculated from 12 to 0 Ma, subject to constant temperature boundary conditions at the base and free surface of the model (Table 4). A basal boundary temperature of 750 °C is applied at 50 km depth below sea level. This temperature is consistent with the peak metamorphic temperatures estimated in most of the Darjeeling-Sikkim Himalaya [*Mottram et al*., 2014b], with temperature at the base of the model in equivalent study in Nepal and Bhutan [*Herman et al*., 2010; *Coutand et al*., 2014] and in geodynamic experiments

[*Beaumont et al*., 2004]. In our experiments, the average crustal geothermal gradient is 15-20 °C/km, which is in the range of the geothermal gradient in the foreland basins of the region estimated to be 20-30 °C/ km [*Rao et al*., 1976; *Zahid et al*., 2005]. Surface temperature decreases with elevation on the model upper surface from 25 °C in the foreland following an atmospheric lapse rate of 6 °C/km [*Naito et al*., 2006]. We use a total simulation time of 12 Ma for two reasons: First, the thermochronometer ages in our dataset are all younger than 12 Ma, recording cooling and exhumation after that time. Second, structural, metamorphic, and geochronological data indicate that the MCT ductile shear zone was still active prior to 10 - 12 Ma, [*Mottram et al*., 2014a; *Mottram et al*., 2015]. The complex kinematics of ductile deformation cannot currently be simulated using the simple fault model in Pecube. We acknowledge that the thermal field at 12 Ma may have been different than in our models if the MCT was still active. If the MCT slip rate at or just prior to 12 Ma was high, temperatures in the MCT hanging wall may have been higher than predicted in the steady-state thermal solution at 12 Ma in our models. This potential underestimation of near-surface temperatures would require more erosion to exhume rocks that cool around 12 Ma in our models compared to nature, for instance. Given the challenge of simulating ductile deformation, we have opted for a simple solution in which the steady-state thermal solution at 12 Ma includes slip along the MHT, which advects heat into the MHT hanging wall and producing at least part of the effect of earlier deformation on the thermal field.

Typical crustal values are used for rock thermal properties in the model (see Table 4 for a complete list of model input parameters; see also *Ehlers*, [2005]), and we invert for the crustal average radiogenic heat production in the range 0-1.5 $\mu W/m^3$. For simplicity, we do not consider the potential thermal influence of ground water flow or fault shear heating on the crustal thermal field.Considering the geological information available for the study area (see section 2) and our own field observations, we chose to test three tectonomorphic scenarios, to

assess the sensitivity of the age data to (1) steady slip on the MHT at steady-state topography, (2) steady slip on the MHT with localized enhanced rock uplift at steady-state topography, (3) steady slip on the MHT with localized enhanced rock uplift at non steady-state topography (40% relief growth between 12 Ma and the present).

The combination of the fault geometries and slip rates defines mass transport in the *Pecube* model domain. Mass is transported parallel to each fault dip panel and the fault geometries are defined by coordinate pairs (*X*, *Z*) that define changes in fault dip at a given horizontal distance from the fault trace and vertical distances above or below sea level (Figure 4). Fault geometries and slip rates do not vary with time in each simulation. Similar to [*Coutand et al*., 2014] and [*Herman et al*., 2010], a constant India-Tibet convergence rate v_{conv} is used with a partitioning factor λ that separates convergence into hanging wall overthrusting $v_{\mathrm{o}} = (1-\lambda)v_{\mathrm{conv}}$ and footwall underthrusting $v_{\mathrm{u}} = \lambda v_{\mathrm{conv}}$ with respect to the model MHT. In addition, faults in the model are kinematically translated to simulate lateral advection of the model topography [*Coutand et al*., 2014; *Whipp et al*., 2009]. Lastly, the northern and southern extent of the model domain was determined based on the geometry of the MHT such that the northernmost cooling ages are exhumed from depths of >10 km and corresponding temperatures well above the effective closure temperature for the ZHe thermochronometer. This results in a planform spatial extent of 100 x 220 km (Table 4).

There are two notable changes in the definition of velocities in our modified version of *Pecube*, compared to that used in [*Coutand et al*., 2014]: (1) kind-band style fold kinematics in the hanging wall block [*Suppe*, 1983], and (2) confining of a zone of enhanced rock uplift to simulate duplex formation [*Herman et al*., 2010]. Kink-band fault kinematics is defined by calculating the location of planes that bisect the angle between any two neighboring fault dip panels and changing the orientation of velocity vectors across those planes rather than using the velocity averaging approach from previous versions of *Pecube* [*Braun et al*., 2012].

Zones of duplex-related enhanced uplift are defined similar to *Herman et al*., [2010] and simulate the long-term exhumation of rock in an active duplex causing a zone of enhanced rock uplift (or localized crustal accretion, labeled CA in Figure 4) coincident, at the end of the run, with the present location of the duplex. The rock uplift enhancement is simply an encoded additional vertical velocity component added to each velocity vector within the zone of crustal accretion, which is defined as the region between two points at specified distances from the fault trace. Rather than simulate the complex tectonic behavior of duplex development, this modification produces the first order effects of enhanced rock uplift and thermal advection in a duplex region (Figure 4).

Inversion of estimated Quaternary fault slip rates and modern interseismic geodetic velocities across the MFT/MHT yield convergence rates of 20 mm/yr along the MFT from eastern Nepal to eastern Bhutan [*Lavé and Avouac*, 2000; *Loveless and Meade*, 2011]. GPS measurements carried out in NE India and Bhutan, indicate that a maximum of 10-20 mm/yr of convergence is being accommodated in the eastern Himalaya [*Mukul*, 2010; *Mukul et al*., 2010; *Vernant et al*., 2014; *Burgess et al*., *2012*] and we use this large range of values. Because our model geometry and the convergence rate are variables in the inversion, we have selected a broad range for the partitioning factor of $\lambda = 0.6 - 0.8$ (Table 4). In our models, we treat the MBT and the MFT as a single structure located at the modern surface trace of the MBT, considering that the two are close (0-10 km in horizontal distance; Figure 1). In addition, reset thermochronologic data along both profiles are restricted to the north of the MBT suggesting the MFT has, so far, little contributed to the Himalayan exhumation. Other than the MHT, we do not simulate movements on hinterland structures including the MCT and the STDS, since there is no evidence for significant displacement on these structures after 12 Ma. We recognize that ductile shearing in the MCT zone may have occurred until 10 Ma [*Mottram et al*., 2014a; *Mottram et al*., 2015], however, since it does not disrupt the cooling

age trend (Figure 3) its Late Miocene activity must have had a limited impact on our thermochronological dataset.

Model topography is either fixed with time and based on modern surface elevations, or allowed to evolve from a geometry in which the peaks are fixed at their present elevations and the valleys have been infilled by 40%. Steady-state model topography is from a Shuttle Radar Topography Mission (SRTM) [*Farr et al*., 2007] 90-m digital elevation model of Sikkim, down sampled to an effective resolution of 900-m (Table 4). The initial low-relief topography of the unsteady-state topography model is produced using the modern topography. In a first step, elevations from the modern topography were averaged in an east-west direction, producing a topographic plane dipping toward the foreland. In a second step, where the elevation of a point in the modern DEM was lower than the average elevation value in that corresponding row, the elevation was increased by 75% of the difference between the average and the modern value. Values higher than the mean, representing local peaks, were left unchanged. The resulting topography retains the peaks of the modern topography but has valley that are filled to 75% of their modern depth below the average elevation value, which corresponds to about 40% of the modern topography.

Flexural isostasy is enabled in our models to simulate changes in rock exhumation rate due to isostatic adjustments as required when topography changes (Table 4). Flexure is simulated as bending of a thin elastic plate and applied incrementally over each model time step. North of the MFT, the elastic effective thickness of the Indian plate inferred from Bouguer anomaly profile ranges between 35-25 km in eastern Nepal [*Berthet et al*., 2013] and 20-15 km in Bhutan [*Hammer et al*., 2013] accordingly, we use a fixed intermediate value of 20 km in Sikkim.

Cooling ages are predicted using the thermochronometer age prediction algorithms available in Pecube; ZHe ages are predicted using the numerical scheme of *Wolf et al*. [1998]

and the kinetic parameters of *Reiners* [2005] and AFT ages are predicted using the linear-fanning model of *Green et al*. [1989] and the kinetic parameters of *Crowley et al*. [1991].

4.2. Inversion algorithm: Neighborhood Algorithm

The thermochronometer age dataset presented in Section 3 is formally inverted using *Pecube* in combination with the Neighborhood Algorithm (NA) [*Rickwood and Sambridge*, 2006; *Sambridge*, 1999a; b] to search and define ranges of input parameters that produce predicted cooling ages consistent with the observed age data. The goal of the data inversion is to define the fault slip rates, slip partitioning and geometry of the MHT, the rate and location of duplex-related enhanced uplift in the LHS and assess whether topographic evolution has an effect on the observed age patterns (Table 5).

The first stage of the Neighborhood Algorithm is a multidimensional parameter search in which parameter combinations are selected to define the ranges that provide the lowest misfit to the observed age data [*Sambridge*, 1999a]. For the first set of forward models, model input parameters are randomly selected from their defined ranges and used to divide the model parameter space into Voronoi cells [*Sambridge*, 1999a]. Input parameters for subsequent forward models are selected from within the subset of Voronoi cells with a low misfit to the observed age data. The misfit is calculated using a goodness-of-fit statistic Φ to compare the predicted and observed cooling ages,

$$\Phi = \frac{1}{n}\sqrt{\sum_{i=1}^{n}\frac{\left(\mathrm{PredAge}_i - \mathrm{ObsAge}_i\right)^2}{\sigma_i^2}} \quad (2)$$

where n is the number of thermochronometer ages, PredAge is the age predicted by Pecube, ObsAge is the observed age and σ is the 1-sigma uncertainty in the observed age. It is worthwhile to note that like *Coutand et al*., [2014], we use the continuous version of the Neighborhood Algorithm [*Rickwood and Sambridge*, 2006], which selects model input parameters for each subsequent forward model from the current Voronoi cells with the lowest

misfits, rather than doing so in discrete iterations. To ensure slow convergence and that all parameter combinations that yield a good fit to the observed ages are considered, input parameters for each forward model are selected from all but the 10% of the Voronoi cells that yielded the worst data misfits. The search converges on a constant low misfit typically after 10,000-15,000 forward models.

The second stage of the Neighborhood Algorithm is an appraisal of the search results to define statistical limits on the ranges of input parameters that provide a good fit to the observed age data [*Sambridge*, 1999b]. Bayesian inference is used to produce posterior probability density functions (PPDFs) for each model parameter using a likelihood function *L*,

$$L = \exp\left(-\frac{n}{2}\sqrt{\sum_{i=1}^{n}\frac{(\mathrm{PredAge}_i-\mathrm{ObsAge}_i)^2}{\sigma_i^2}}\right). \quad (3)$$

The appraisal yields 1D and 2D PPDFs for the model parameters that are presented for each set of model parameters in Section 5

5. Modeling Results

Approximately 30 inversions were run in this study, with an average calculation time of three-four weeks for each inversion on the *Glooscap* cluster (*ACEnet* consortium) based at Dalhousie University. The aim of this extensive modeling work was to investigate a wide range of tectonomorphic scenarios. In this manuscript we have chosen to present only three inversions of the tectonomorphic scenarios most consistent with independent geological constraints. For details on model input values, see section 4 and Table 5.

5.1. Inversion set SIK01: Constant slip rate on the MHT with steady-state topography

In this first inversion, we test the model's ability to reproduce observed age pattern for a scenario involving constant slip rate on the MHT during the last 12 Ma at topographic steady state. This inversion set comprises 13314 forward models (convergence occurred after ~

10,000 models), the lowest-misfit value is 1.06 and the free parameters values for the lowest-misfit solution are found in Table 5.

The results of the inversion (Figure 5) indicate that the age dataset is mainly sensitive to the fault kinematic parameters with the NA appraisal producing exponential-shaped 1D PPDFs for υ_{conv} and λ (Figure 5c). The convergence rate is well defined at values between 17-20 mm/yr as is the partitioning factor at low values between 0.6-0.65. Taken together, these values yield high overthrusting rate ranging from 6-8 mm/yr, in the higher range of previous studies [*Coutand et al*., 2014; *Herman et al*., 2010; *Robert et al*., 2011; *Whipp et al*., 2007] suggesting the system requires rapid heat advection in the hanging wall of the MHT to reproduce the measured age pattern. This is supported by the high best-fit value for the radiogenic heat production ($A = 19.9$ °C/Myr), further heating the upper crust (Table 5). The geometry of the MHT in the frontal part of the range, defines a 35-km-long shallowly northward dipping (2°) segment at depths of 9 to 10 km (Figures 5a & b, 8d), consistent with geophysical data [*Acton et al*., 2011], but 1-2 km deeper than estimated by cross-section balancing [*Bhattacharyya and Mitra*, 2009] (Figure 2). However, the NA appraisal stage results yields flat 1D PPDFs with large 1σ errors spanning the entire parameter range for these free parameters (Figures 5a & b). In spite of the good convergence obtained through the search, the geometrical parameters (X_2, Z_2) and (X_3, Z_3) remain poorly resolved. This poor resolution appears to result from the inability of the models in this inversion set to reproduce ages that are young enough in the central latitudes of the study area and old enough further north (e.g. Figure 8a).

The results highlight the significant tectonic/advective perturbation of the crustal isotherms, which induces substantial variations in the geothermal gradient along the transect (Figure 8d). Predicted mean surface heat flow vary from 46.6 ± 1.2 mW/m^2 in the foreland to 116.1 ± 16.4 mW/m^2 in the hinterland. The former is consistent with the heat flow in the

Indian basement, although the values in NE India are slightly higher at ~60 - 80 mW/m^2 [*Roy and Rao*, 2000]. Elsewhere in the Himalaya, surface heat flow has only been measured in hotsprings and the estimated values of nearly 200 mW/m^2 [*Derry et al*., 2009] are most likely not representative of the rest of the orogenic wedge. Surface heat flow from our experiments in the hinterland is however consistent with heat flow values of 90-100 mW/m^2 in southern Tibet, north of Bhutan [*Francheteau et al*., 1984]. Predicted ages obtained from a single high-resolution forward model using the parameters yielding the lowest misfit value moderately to poorly match AFT, and ZHe data (Figure 8a). The high overthrusting rate and high heat production appear to be required to produce the young AFT ages in the southern parts of the Sikkim region, however this results in ages that are younger than the observed AFT ages in the north. This combination also produces ZHe ages that are too young in the southern portion of the study area. Combined, this suggests that an important component is missing in the exhumation and cooling of the observed ages.

5.2. Inversion set SIK02: Constant slip rate on the MHT and localized enhanced rock uplift at steady-state topography

In a second inversion, we test a tectonomorphic scenario involving constant slip rate on the MHT coupled with localized enhanced rock uplift during the last 12 Ma at topographic steady state (Table 5). We introduce a zone of enhanced basal accretion centered on the modern location of the LHD, with northern and southern boundaries free to move (Figure 4).

This inversion set comprises 21020 forward models that converged toward a lowest-misfit value of 0.52, which is the best value for the 30 scenarios tested in this study (Figure 6). For the lowest misfit forward model, υ_{conv} converged toward a relatively low value of 12 mm/yr but remains poorly resolved with a very large asymmetric 1σ error, while the NA appraisal produced half-Gaussian-shaped 1D PPDFs for λ with a peak value of 0.6 (Figure 6c). These values yield an overthrusting rate of about 5 mm/yr. The posterior model correlation matrix

clearly indicates that there is an anti-correlation between these two parameters (Figure S4 in Supplementary Material).

The MHT geometry in SIK02 is rather different from SIK01 with a much less pronounced mid-crustal ramp. In the frontal part of the range, the MHT dips northward at 19° down to a depth of 6.5 km (Figures 6a and 8e) and then remains straight dipping northward at 10° until a depth of 29 km in the range of values proposed by [*Bhattacharyya and Mitra*, 2009]. In this inversion again, the NA appraisal stage results yield flat 1D PPDFs (Figures 6a & b) indicating that the geometrical parameters (X_2, Z_2) and (X_3, Z_3) are poorly resolved. In contrast, 1D PPDFs of the free parameters related to the area and the rate of enhanced crustal accretion have half-Gaussian (for the northern boundary of the accretion zone, CA_{prox}) and Gaussian shapes (for the southern boundary for the accretion zone, CA_{dist} and the uplift rate, υ_{CA}), which indicates that they are well-constrained (Figures 6d & e). Within 1σ error, the zone of enhanced crustal accretion is located between 15-32 km and 60-70 km north of the surface trace of the MBT with lowest misfit values at 25 and 69 km for the southern and northern boundary, respectively (Figures 6d & 8e). υ_{CA} is well-constrained at 2.3 mm/yr with a 1σ error of ~ 2 mm/yr (Figure 6e). Combined, the lack of resolution of the fault parameters and well-resolved duplex parameters suggests that duplex-related uplift and exhumation is an important component of the cooling of samples within the Rangit and Tista windows, dominating the influence of the underlying MHT geometry. This is not surprising as thrust motion along the shallow dip of the MHT beneath the windows (~11°) will result in uplift velocities of <1 mm/yr whereas the duplex-related uplift velocity is more than double that value (2.3 mm/yr).

Predicted mean surface heat flow vary from 50.8 ± 1.4 mW/m^2 in the foreland to 91.4 ± 12.6 mW/m^2 in the hinterland (Figure 8e) and the predicted cooling ages fit well to the observed age data. The preferred radiogenic heat production value from this inversion is still

fairly high (16.1 °C/Myr), but slightly lower than in SIK01 suggesting that thermal advection owing to duplex-related uplift reduces the need for very high radiogenic heat production values (Figure 6e; Table 5). The peak of the 1D PPDF for heat production is also broad, indicating a relatively low sensitivity to this parameter. Predicted ages obtained from a high-resolution forward model using the parameters yielding the lowest misfit match the observed data very well except for the northernmost AFT age which yields a predicted age 7 Ma younger than the measured age and, the southernmost ZHe data point with 2.5 Ma difference between predicted and measured ages (Figure 8b). The northernmost AFT cooling age (sample SK55 in Kellett et al., 2013) is consistently poorly reproduced in our models because it most likely results from a fast cooling episode associated with tectonic denudation, cessation of activity and ensuing thermal relaxation in the footwall of the STDS 14-13 Ma ago [*Kellett et al*., 2013]. Preservation of this old AFT cooling age in the modern landscape, suggests that since 12 Ma (when our runs start), less denudation has occurred at these high elevations than further south along the transect.

5.3. Inversion set SIK03: Constant slip rate on the MHT, localized enhanced rock uplift and evolving topography

In central Sikkim, the deep erosion of the GHS nappe by the Rangit and Tista rivers has exposed the underlying LHS in a tectonic window and has deeply dissected the modern landscape. To quantify the potential influence of progressive relief growth on the age distribution, we test in this third inversion a tectonomorphic scenario similar to model SIK02 with an initial topography that has ~ 40% less relief than the modern topography, and which evolves linearly toward the present-day topography over 12 Ma. We assume that relief increases as a result of preferential valley incision, with the peaks fixed at their current elevation and the valley bottom progressively lowered through incision. This implies higher exhumation rates in the valleys than on the ridges.

This inversion set comprises 21020 forward models that converged toward an excellent lowest-misfit value of 0.54. The results are nearly identical to those in inversion SIK02 (Figures 6 & 7). The convergence rate remains poorly resolved with a best-fit value of 12.2 mm/yr and a partitioning factor well-defined at 0.6-0.63 (Figure 7c). The NA appraisal stage again yields flat 1D PPDFs for the four free geometric parameters (Figures 7a & b), leaving the frontal geometry of the MHT poorly constrained. Within 1σ error, the zone of enhanced crustal accretion is comprised between 15-35 km and 60-70 km north of the surface trace of the MBT with lowest misfit values at 22.3 and 69 km (Figures 6d & 8e). υ_{CA} is well-constrained at 2.2 mm/yr, similar to inversion SIK02, with an associated 1σ error of about 2 mm/yr (Figure 7e). As for inversion SIK02, the well-defined range of duplex variables and lack of resolution for the MHT geometry indicates that the cooling ages are strongly affected by duplex-related exhumation. Furthermore, the relative lack of sensitivity to the evolving topography emphasizes the influence of duplex uplift and exhumation, though the linear change in model topography over 12 Ma results in a quite slow rate of topographic change and the effects of topographic evolution would be more significant if the topography was to evolve over a much shorter time scale.

The predicted mean surface heat flow is slightly lower than in SIK02, from 46.5 ± 1.9 mW/m^2 in the foreland to 84 ± 14.1 mW/m^2 in the hinterland, and the fit of the predicted ages to the observed is nearly identical. The best-fit radiogenic heat production value (13.5 °C/Myr) has again decreased slightly as reflected in the lower surface heat flow, and this reduction again supports the role of duplex growth and thermal advection in producing young cooling ages in and proximal to the Rangit and Tista windows (Figure 7e; Table 5). Predicted ages obtained from a high-resolution forward model match very-well with observed AFT, and ZHe data except, similarly as in the previous scenario, for the northernmost AFT age which yields a predicted age 7.5 Ma younger than the measured age and, the southern and

northernmost ZHe datapoint with 2 to 3 Ma difference between predicted and measured ages, respectively (Figure 8c).

6. Discussion

6.1. Kinematic approach in modeling duplex structures

The presence and importance of duplex structures in the LHS have long been recognized along the Himalayan arc [e.g. *Bhattacharyya and Mitra*, 2009; *DeCelles et al*., 2001; *He et al*., 2015; *Long et al*., 2011a; *McQuarrie et al*., 2008; *Robinson et al*., 2001; *Robinson and Martin,* 2014; *Schelling and Arita*, 1991; *Srivastava and Mitra*, 1994]. The extent to which the formation of these structures has impacted the upper-crustal thermal field and the exhumation of the range front has been diversely assessed by thermo-kinematic modeling studies in NW India [*Célérier et al., 2009*], Nepal [*Bollinger et al*., 2004; *Bollinger et al*., 2006; *Herman et al*., 2010] and in eastern Bhutan [*McQuarrie and Ehlers*, 2015]. Though different options exist for modeling duplex deformation and rock uplift, all models share the key component of mass transfer from the down-going Indian plate across the MHT into the hanging wall. This results in "hairpin" trajectories of rock particles as they cross the MHT in the zone of enhanced duplex-driven rock uplift (Figure 4).

In this study, we have opted for a simple model of duplex-driven uplift wherein the vertical uplift of rock in both the footwall and hanging wall increases in the duplex zone, which has advantages and disadvantages compared to the more complex duplex kinematics used by [*McQuarrie and Ehlers*, 2015]. Our approach is the same as is summarized in *Avouac*, [2007] and adopted by *Herman et al*., [2010] and involves the underthrusting and overthrusting of the footwall and hangingwall of the MHT, respectively, and the localized and continuous basal accretion of the underthrusted plate across the MHT with a fixed geometry. In our models, the zone of basal accretion is fixed with respect to the laterally advected topography, and as a result, it is progressively translated southwards along the MHT

during the run. This permits transfer of material from the down-going plate into the overriding plate by allowing particles to cross the basal décollement at progressively more southern parts of the fault through time, simulating the duplex propagation toward the foreland. This approach is flexible and allows changes in the fault displacement rates through time during time windows specified in our inversions.

The interpretative balanced cross-section approach used by *McQuarrie and Ehlers*, [2015] involves incremental reconstruction of fault geometries and propagation rates through time, which is linked to a thermal model to predict cooling ages at different deformation stages of a range front. This approach is promising and quite powerful in the context of thin-skinned fold-and-thrust belts, where cross-section balancing requirements [*Woodward et al*., 1989] are met. For instance, the impact of various duplex formation scenarios could be considered with this approach. While true for many thin-skinned fold-and-thrust belts, cross-section balancing requirements are not satisfied in the metamorphic terranes like the Himalaya because the GHS is made up of high metamorphic grade rocks, characterized by pervasive ductile deformation, heterogeneous volume changes due to partial melting, melt segregation and magmatism, foliation transposition, passive shear folds, folds with hinges parallel to the direction of tectonic transport (e.g. *Godin et al*., 2006; *Grujic et al*., 1996). The greenschist metamorphic grade LHS rocks have also developed foliations and experienced intense amounts of general shear, and the basement itself might have been deformed when underthrusted under the belt [*Avouac*, 2007]. In our opinion, these facts complicate the use of detailed kinematic reconstructions along the Himalayan arc and we therefore have opted for the simple duplex model described above.

6.2. Influence of localized enhanced rock uplift (duplex formation): Inversions SIK01 versus SIK02

Inversion SIK01 involving only steady displacement on the MHT clearly fails to reproduce the observed cooling age pattern, while inversion SIK02 provides a much better fit to the data (Figures 8a & 8b). Though the formation of duplexes is clearly documented in the LHS in Sikkim [*Bhattacharyya and Mitra*, 2009; *Mitra et al*., 2010], the results of inversion SIK01 further support the notion that it is difficult to heat the MHT hanging wall via thermal advection, exhume rocks rapidly, and produce the observed young cooling ages without a zone of enhanced rock uplift in the duplex region. For example, inversion SIK01 returns high values of volumetric heat production (20 °C/Myr ≈ 1.4 mW/m^3), total convergence (≈ 20 mm/yr) and low values of convergence partitioning (≈ 0.6) that produce overthrusting values (8 mm/yr) exceeding those found by equivalent studies elsewhere [*Coutand et al*., 2014; *Herman et al*., 2010]. It is worth noting that the model cannot compensate this situation by flattening the MHT north of 27.5°N, since points 4 and 5 are kept fixed based on geophysical data. In contrast, localized basal accretion in model SIK02 diverts the footwall particle path upward across the MHT and advects heat across the décollement. This results in overthrusting rates within the range predicted by previous studies (~ 5 mm/yr) and a model that closely reproduces the inverted bell pattern of the cooling ages (Figure 8b).

Duplexes have also been well documented in the LHS of Bhutan [*Long et al*., 2011a; *Long et al*., 2011b; *McQuarrie et al*., 2008; *Tobgay et al*., *2012*], but there, thermochronogical data modeling similar to that described in this paper has, so far, failed to demonstrate a significant impact of duplex formation on the distribution of low-temperature thermochronometric ages [*Coutand et al*., 2014]. However, the structural units exposed in the Paro window (underneath which the western Bhutan duplex has developed) are equivalents to the MCT zone of Sikkim, which indicates that the magnitude of exhumation in the Tista-Rangit double window is much

larger than that in the Paro window. In eastern Bhutan where the Kuru Chu duplex is deeply incised, recent 3D thermo-kinematic modeling implemented by new geophysical constraints on the MHT geometry [*Singer et al*., 2015] demonstrates the impact of duplex formation on the distribution of peak temperatures in rocks exposed along the transect [*Grujic et al*., 2016]. These contrasting modeling results show that even when duplexes are documented in the field, the impact of their structural development on low-temperature cooling age distributions may be hard to detect when the magnitude of exhumation has been too low to expose the deeper part of the duplexes.

6.3. Late Neogene exhumation rates in the Sikkim Himalaya

Long-term exhumation rates represent the average rate of depth decrease since a given sample crossed the closure temperature of either AFT or ZHe systems; a calculation usually performed with an assumed ambient geothermal gradient and without geobarometry. Sometimes, long-term exhumation rates may have different values for different thermochronometers on a single sample because crustal trajectories dictated by the kinematics, fault geometry and enhanced rock uplift zone in the model change over time and closure isotherms are not flat [see *Coutand et al*., *2014*]. Long-term exhumation rates calculated from the lowest-misfit forward model yielded by inversion SIK02 indicate there are three domains which, from south to north are characterized by long-term exhumation rates of 1.1-1.2 mm/yr south of 27.1 °N, ~2.6-3.5 mm/yr between 27.1 °N and 27.5 °N, and 1.2 decreasing to 0.6 mm/yr north of 27.5 °N (Figure 9d). However in detail, our models yield complex time-Temperature-Depth histories (Figures 9a-c). The points located today to the south of the duplex (south of 27.1°N), have always remained in the southern part of the hangingwall of the northward migrating MHT/MBT, yet have not been caught into the enhanced rock uplift zone. These points have undergone rather monotonous cooling and exhumation histories during the model evolution (Figure 9a) with long-term exhumation rates

of 1.15 ± 0.04 mm/yr accelerating to 1.66±0.02 mm/yr over the last 1 Ma when the particles travel on top of the frontal ramp just before they become exposed to the surface. The Temperature-Depth paths correspond to a geothermal gradient of ~20 °C/km.

The points that have been caught into the duplex zone were originally located in the footwall of the MHT and followed time-Temperature-Depth paths that progressively change from north to south but have the same pattern (Figure 9b). All the points were initially buried to progressively greater depths from south to north and diachronously started to exhume from the north to the south, which is consistent with the development of a foreland propagating duplex. These displacements paths result in Temperature-Depth loops with a "prograde" segment corresponding to a geothermal gradient of ~20 °C/km and the exhumation path along a geothermal gradient of ~35 °C/km. The northernmost points resided at a nearly constant depth, yet accompanied by heating, which was caused by sub-horizontal translation across the deformed isotherms. This period lasted ca. 2 Ma in the north and nearly disappears for the southernmost points, yielding progressively tighter Time-Depth loops towards the south. The exhumation path is monotonous for all the points and progressively increases from 2.6 mm/yr in the south to 3.5 mm/yr in the north. In the duplex zone, the onset of cooling and exhumation occurs when the points from the footwall of the MHT cross it and become accreted to its hangingwall.

The points located north of ~27.5°N (yellow lines in Figure 9c), have followed a two to three-stage exhumation path, slow in the middle at 0.4 mm/yr and fast at the beginning and the end at 1.20 ± 0.04 mm/yr. These points remained in the MHT hangingwall during the entire run and the transitions in exhumation rates correspond to the MHT ramp-flat-ramp segments passages. All the points now at the surface started from approximately similar depths of ~ 12 km, but the slow exhumation stage occurred at greater temperature and earlier

in the south than in the north. The entire time-depth paths occured along a geothermal gradient of ~35 °C/km.

Recent study involving detrital AFT thermochronology of 10 sub-basins distributed along the Tista river drainage [*Abrahami et al*., 2016] provides catchment-averaged exhumation rates gradually decreasing northwards from 1.20 ± 0.63 to 0.51 ± 0.21 mm/yr (white circles in Figure 9). Long-term exhumation rates extracted from this detrital thermochronometric dataset do not correlate with either geomorphic or climatic proxies suggesting that the thermochronometric signal is primarily the result of tectonic processes [*Abrahami et al*., 2016]. When comparing our results, we notice that long-term exhumation rates derived from *in situ* and detrital samples are in good agreement outside of the Tista-Rangit double window but differ by 2-2.5 mm/yr within it (Figure 9d). This difference may result from the fact that the detrital samples 1) were collected at catchment outlets located on the outskirt of the Tista window (none of them draining the window alone), and 2) integrate data over wide, geologically and geomorphologically heterogeneous areas. The resulting thermochronometric signals may have missed significant fractions of young cooling ages preferentially located in the core of window and/or have masked the youngest ages by averaging them at the scale of large catchments.

6.4. Influence of evolving topography: Models SIK02 versus SIK03

Topography influences near-surface isotherms to depths that depend on both its amplitude and the wavelength (e.g. *Braun*, 2002; *Mancktelow and Grasemann*, 1997; *Stüwe and Hintermüller*, 2000; *Stüwe et al*., 1994). Hence, a change in surface topography through time will transiently perturb the near-surface crustal thermal field and, consequently, affect the distribution of cooling ages at the surface, for thermochronometric systems that are sensitive to those temperatures. In order to evaluate the impact of multi-kilometric incision by the Tista and Rangit rivers in Sikkim on our age data, we have run several inversions in which relief

increases through time. Obviously, it is difficult to determine how topography has changed over the last 12 Ma, both in terms of relief-amplitude, incision rates and positions of major Himalayan drainage basins. For the latter, it has been suggested from past and present location of fluvial megafans in the Ganges basin that rivers draining the Himalaya toward the foreland have flowed along similar pathways for several millions of years [*Gupta*, 1997]. For the former points, however, there are no constraints, so we have to select a reasonable topographic evolution scenario. In the absence of paleotopographic constraints and for sake of simplicity, we assume that the relief increase occurred through progressive valley incision, where valley bottoms were lowered while peaks remained at a constant modern elevation. For example, inversion SIK03 has a significant ~ 40% increase in relief. Our models do not include the effect of fluid flow in the uppermost crust, which could dampen the effects of the shape of the topography on the underlying isotherms [*Whipp and Ehlers*, 2007].

Both inversions at steady (SIK02) and changing topography (SIK03) converge on lowest misfits (~ 0.5) for similar parameter values (Table 5), suggesting that the progressive topographic growth had a limited impact on the cooling age distribution. In model SIK03, the maximum relief gain is recorded at the confluence between the Talong and the Tista rivers, just north of Mangan (Figure 1) and reaches ~ 3 km over 12 Ma, which averages to 0.25 mm/yr, a rate slower than the slowest exhumation rates documented in northern Sikkim (0.6 mm/yr; Figure 9). *Valla et al*., [2010] have shown that relief development must be 2-3 times faster than the background exhumation/erosion rate to be recorded and quantitatively extracted from thermochronological data. Therefore, we conclude that in Sikkim, relief gain through fluvial incision is at best, 5 times too slow with respect to background exhumation rate, to be recorded in thermochronological data.

7. Conclusions

Our analysis of 34 new apatite fission track and zircon (U-Th)/He bedrock samples from the Sikkim Himalaya combined with 3D thermokinematic modeling of the thermochronological dataset constrained by geological and geophysical independent observations lead us to the following conclusions:

1- When plotted against latitude, parallel to the Himalayan tectonic transport direction, thermochronological dataset defines a symmetrical concave-up pattern between the MBT and the STDS, with ages ranging from 12-13 Ma at the northern and southern extremities to ~ 1 Ma in the center of the transect. The cooling ages do not correlate with topography, rainfall distribution and the deeply incised high-relief Tista window, suggesting that tectonic processes exert a dominant influence on their distribution.

2- When inverted using a 3D thermokinematic model, this thermochronological dataset is most compatible with a tectonic model involving the growth of a duplex in the upper crust accompanied by a steady displacement on the basal décollement during the last 12 Ma at steady-state topography. Localized rock uplift caused by near-vertical accretion across the MHT and simulating forelandward propagating duplex formation occurs at a rate of ~ 2.3 mm/yr, in a zone located between 25-70 km north of the surface trace of the MBT, moving southward at a rate of 4.8 mm/yr with respect to the MHT during the run.

3- Long-term exhumation rates vary along the transect, from 1.1-1.2 mm/yr south of 27.1 °N, 2.6-3.5 mm/yr in the duplex domain, and decrease from 1.2 to 0.6 mm/yr to the north of the duplex. The highest exhumation rates are centered on the zone of enhanced rock uplift caused by duplex formation.

4- Time-Temperature-Depth particle paths are complex and indicate that exhumation rates have varied over time. Points to the south of the duplex have undergone monotonous exhumation histories ranging from 1.1 – 1.6 mm/yr. Points in the duplex have undergone a

clockwise temperature loop, reflecting the burial, accretion to the MHT hanging wall and exhumation. As a result, the Temperature-Depth loops become progressively tighter and younger southward and the exhumation rates slower (3.5-2.6 mm/yr). Finally the points to the north of the duplex have undergone a progressive, stepwise exhumation history reflecting their trajectories over the MHT succession of ramps and flats; with early and latest stages of exhumations at 1.2 mm/yr and intermediate exhumation rate at 0.4 mm/yr.

5- Relief growth has likely happened through fluvial incision by the Tista and Rangit rivers during the Late Neogene. However, our dataset cannot quantify the timing and magnitude of this relief change because the closure temperatures of the applied thermochronometers are too high to be sensitive to relief change and/or the rate of relief change was too slow.

6- In Darjeeling-Sikkim Himalaya, our modeling results demonstrate a prominent impact of duplex formation on the distribution of low-temperature thermochronometric ages while this does not seem to be the case in Bhutan [*Coutand et al.,* 2014]. These contrasting modeling results show that even when duplexes are documented in the field, as is the case in both Bhutan and Sikkim, the impact of their structural development on low-temperature cooling age distributions may be difficult to detect when the magnitude of exhumation has been too low to expose the deeper part of the duplexes.

7- Overall, our modeling results are in agreement with equivalent studies in the Bhutan, Nepal and NW Indian Himalaya [*Whipp et al.,* 2007; *Célérier et al.,* 2009; *Herman et al.,* 2010; *Robert et al.,* 2010; *Coutand et al.,* 2014; *McQuarrie and Ehlers*, 2015]. All the experiments demonstrate that, both across and along the strike of the orogen, the variations in upper crustal exhumation rates are primarily caused by the geometry and kinematics of the basal décollement locally associated with duplex formation.

Acknowledgments

Discussions with K. Bhattacharyya, F. Herman, D. Kellett, and M. Mukul are greatly appreciated. B. Bookhagen kindly provided the rainfall profile in Figure 3. Constructive reviews by P. Valla and an anonymous reviewer have improved a previous version of the manuscript. We acknowledge editorial handling by M. Jolivet. IC thanks financial support from the France-Stanford Foundation, and the Natural Sciences and Engineering Research Council of Canada (Discovery grant RGPIN 371671). KL Master Thesis analytical work was partly supported by the Shell Experiential Learning Fund (SELF). The new thermochronological datasets used in this manuscript are available in Tables 2 and 3. AFT counting dataset is available upon request to the corresponding author (IC).

References

Abrahami, R., P. van der Beek, P. Huyghe, E. Hardwick, and J. Carcaillet (2016), Decoupling of long-term exhumation and short-term erosion rates in the Sikkim Himalaya, *Earth and Planetary Science Letters*, *433*, 76-88.

Acharyya, S. (1971), Structure and stratigraphy of the Darjeeling frontal zone, eastern Himalaya, *Rep*., 71-90 pp, Geological Survey of India.

Acharyya, S. K., and K. K. Ray (1977), *Geology of the Darjeeling-Sikkim Himalaya*. *Guide to excursion n°3*., 1-25 pp., Geological Survey of India, Calcutta.

Acton, C. E., K. Priestley, S. Mitra, and V. K. Gaur (2011), Crustal structure of the Darjeeling–Sikkim Himalaya and southern Tibet, *Geophysical Journal International*, *184*(2), 829-852.

Adlakha, V., K. A. Lang, R. C. Patel, N. Lal, and K. W. Huntington (2013), Rapid long-term erosion in the rain shadow of the Shillong Plateau, Eastern Himalaya, *Tectonophysics*, *582*, 76-83.

Alsdorf, D., et al. (1998), INDEPTH (International Deep Profiling of Tibet and the Himalaya) multichannel seismic reflection data: description and availability, *Journal of Geophysical Research*, *103*(B11), 26,993-926,999.

Anczkiewicz, R., S. Chakraborty, S. Dasgupta, D. Mukhopadhyay, and K. Kołtonik (2014), Timing, duration and inversion of prograde Barrovian metamorphism constrained by high resolution Lu–Hf garnet dating: A case study from the Sikkim Himalaya, NE India, *Earth and Planetary Science Letters*, *407*, 70-81.

Avouac, J.-P. (2003), Mountain Building, Erosion, and the Seismic Cycle in the Nepal Himalaya, in *Advances in Geophysics*, edited, pp. 1-80, Elsevier.

Avouac, J.-P. (2007), Mountain building: From earthquake to geological deformation, *Dynamic processes in extensional and compressional settings: Treatise on Geophysics*, *6*, 377-439.

Beaumont, C., R. A. Jamieson, M. H. Nguyen, S. Medvedev (2004), Crustal channel flows: 1. Numerical models with applications to the tectonics of the Himalayan‐Tibetan orogeny, *Journal of Geophysical Research*, 109, B06406.

Berthet, T., G. Hetényi, R. Cattin, S. Saptoka, C. Champollion, T. Kandel, E. Doerflinger, D. Drukpa, S. Lechmann, and M. Bonnin (2013), Lateral uniformity of India Plate strength over central and eastern Nepal, *Geophysical Journal International*, doi: 10.1093/gji/ggt357.

Bhattacharyya, K., and G. Mitra (2009), A new kinematic evolutionary model for the growth of a duplex — an example from the Rangit duplex, Sikkim Himalaya, India, *Gondwana Research*, *16*(3-4), 697-715.

Bhattacharyya, K., and G. Mitra (2011), Strain softening along the MCT zone from the Sikkim Himalaya: relative roles of quartz and micas, *Journal of Structural Geology*, *33*, 1105-1121.

Biswas, S., I. Coutand, D. Grujic, C. Hager, D. Stockli, and B. Grasemann (2007), Exhumation and uplift of the Shillong plateau and its influence on the eastern Himalayas: New constraints from apatite and zircon (U- Th- [Sm])/He and apatite fission track analyses, *Tectonics*, *26*(6), TC6013, doi:10.1029/2007TC002125.

Bollinger, L., J.-P. Avouac, O. Beyssac, E. J. Catlos, T. M. Harrison, M. Grove, B. Goffe, and S. Sapkota (2004), Thermal structure and exhumation history of the Lesser Himalaya in central Nepal, *Tectonics*, *23*(5), TC5015.

Bollinger, L., P. Henry, and J.-P. Avouac (2006), Mountain building in the Nepal Himalaya: Thermal and kinematic model, *Earth and Planetary Science Letters*, *244*(1), 58-71.

Bookhagen, B., and D. W. Burbank (2010), Toward a complete Himalayan hydrological budget: Spatiotemporal distribution of snowmelt and rainfall and their impact on river discharge, *Journal of Geophysical Research*, *115*(F3), F03019.

Braun, J. (2002), Quantifying the effect of recent relief changes on age–elevation relationships, *Earth and Planetary Science Letters*, *200*, 331-343.

Braun, J. (2003), Pecube: a new finite-element code to solve the 3D heat transport equation including the effects of a time-varying, finite amplitude surface topography, *Computers and Geosciences*, *29*, 787-794.

Braun, J. (2005), Quantitative constraints on the rate of landform evolution derived from low-temperature thermochronology, *Reviews in Mineralogy and Geochemistry*, *58*(1), 351-374.

Braun, J., P. Van Der Beek, P. Valla, X. Robert, F. Herman, C. Glotzbach, V. Pedersen, C. Perry, T. Simon-Labric, and C. Prigent (2012), Quantifying rates of landscape evolution and tectonic processes by thermochronology and numerical modeling of crustal heat transport using PECUBE, *Tectonophysics*, *524-525*(C), 1-28.

Burchfiel, B. C., and L. H. Royden (1985), North-south extension within the convergent Himalayan region, *geology*, *13*(10), 679-682.

Burg, J. P., M. Brunel, D. Gapais, G. M. Chen, and G. H. Liu (1984), Deformation of leucogranites of the crystalline Main Central Sheet in southern Tibet (China), *6*(5), 535-542.

Burgess, W. P., A. Yin, C. S. Dubey, Z-K Shen, and T. K. Kelty (2012), Holocene shortening across the Main Frontal Thrust zone in the eastern Himalaya, *Earth and Planetary Science Letters*, 357, 152-167

Catlos, E., T. Harrison, and M. Kohn (2001), Geochronologic and thermobarometric constraints on the evolution of the Main Central Thrust, central Nepal Himalaya, *Journal of Geophysical Research - Solid Earth*, *106*, 16177-16204.

Catlos, E. J., C. S. Dubey, T. M. Harrison, and M. A. Edwards (2004), Late Miocene movement within the Himalayan Main Central Thrust shear zone, Sikkim, north-east India, *Journal of Metamorphic Geology*, *22*(3), 207-226.

Chakraborty, S., S. Dasgupta, and S. Neogi (2003), Generation of migmatites and the nature of partial melting in a continental collision zone setting: an example from the Sikkim Himalaya, *Indian Journal of Geology*, *75*, 38-53.

Célérier, J., T. M. Harrison, O. Beyssac, F. Herman, W. Dunlap, A. Webb (2009), The Kumaun and Garwhal Lesser Himalaya, India: Part 2. Thermal and deformation histories, *Geological Society of America Bulletin*, 121, 1281-1297.

Clark, M. K., and R. Bilham (2008), Miocene rise of the Shillong Plateau and the beginning of the end for the Eastern Himalaya, *Earth and Planetary Science Letters*, *269*(3), 337-351, doi:10.1016/j.epsl.2008.01.045.

Coutand, I., D. M. Whipp Jr., D. Grujic, M. Bernet, M. G. Fellin, B. Bookhagen, K. R. Landry, and C. Duncan (2014), Geometry and kinematics of the Main Himalayan Thrust and Neogene crustal exhumation in the Bhutanese Himalaya derived from the inversion of multithermochronologic data, *Journal of Geophysical Research - Solid Earth*, *119(2)*, 1446-1481.

Crowley, K., Cameron, M., Schaefer, R. (1991), Experimental studies of annealing of etched fission tracks in fluorapatite, *Geochimica et Cosmochimica Acta,* 89, 1449–1465.

Dasgupta, S., J. Ganguly, and S. Neogi (2004), Inverted metamorphic sequence in the Sikkim Himalayas: crystallization history, P–T gradient and implications, *Journal of Metamorphic Geology*, *22*(5), 395-412.

Davidson, C., D. Grujic, L. S. Hollister, and S. M. Schmid (1997), Metamorphic reactions related to decompression and synkinematic intrusion of leucogranite, High Himalayan Crystallines, Bhutan, *Journal of Metamorphic Geology*, *15*, 593-612.

DeCelles, P. G., G. E. Gehrels, J. Quade, T. P. Ojha, P. A. Kapp, and B. N. Upreti (1998), Neogene foreland basin deposits, erosional unroofing, and the kinematic history of the Himalayan fold-thrust belt, western Nepal, *Geological Society of America Bulletin*, *110*(1), 2-21.

DeCelles, P. G., D. M. Robinson, J. Quade, T. P. Ojha, C. N. Garzione, P. Copeland, and B. N. Upreti (2001), Stratigraphy, structure, and tectonic evolution of the Himalayan fold- thrust belt in western Nepal, *Tectonics*, *20*(4), 487-509.

Derry, L.A., M. J. Evans, R. Darling, and C. France-Lanord (2009), Hydrothermal heat flow near the Main Central thrust, central Nepal Himalaya, *Earth and Planetary Science Letters*, *286*(1), 101-109

Donelick, R. A., P. B. O'Sullivan, and R. A. Ketcham (2005), Apatite fission-track analysis, *Reviews in Mineralogy and Geochemistry*, *58*(1), 49-94.

Duncan, C., J. Masek, and E. Fielding (2003), How steep are the Himalaya? Characteristics and implications of along-strike topographic variations, *Geology*, *31*(1), 75-78.

Ehlers, T. A. (2005), Crustal thermal processes and the interpretation of thermochronometer data, *Reviews in Mineralogy and Geochemistry*, *58*(1), 315-350.

Farr, T. G., et al. (2007), The Shuttle Radar Topographic Mission, *Reviews of Geophysics*, *45*(2), RG2004.

Francheteau, J., C. Jaupart, S. Xian Jie, K. Wen-Hua, L. De-Lu, B. Jia-Chi, W. Hung-Pin, and D. Hsia-Yeu, (1984), High heat flow in southern Tibet, *Nature*, 307, 32-36

Gaetani, M., and E. Garzanti (1991), Multicyclic history of the Northern India continental margin (Northwestern Himalaya), *AAPG Bulletin*, *75*(9), 1427-1446.

Gaidies, F., A. Petley- Ragan, S. Chakraborty, S. Dasgupta, and P. Jones (2015), Constraining the conditions of Barrovian metamorphism in Sikkim, India: P–T–t paths of garnet crystallization in the Lesser Himalayan Belt, *Journal of Metamorphic Geology*, *33*(1), 23-44.

Ganguly, J., S. Dasgupta, W. Cheng, and S. Neogi (2000), Exhumation history of a section of the Sikkim Himalayas, India: records in the metamorphic equilibria and compositional zoning of garnet, *Earth and Planetary Science Letters*, *183*, 471-486.

Gansser, A. (1964), *Geology of the Himalayas*, 289 pp., Interscience Publishers, London and New York.

Garzanti, E. (1999), Stratigraphy and sedimentary history of the Nepal Tethys Himalaya passive margin, *Journal of Asian Earth Sciences, 17(5)*, 805-827.

Godin, L., D. Grujic, R. D. Law, and M. P. Searle (2006), Channel flow, ductile extrusion and exhumation in continental collision zones: an introduction, *Geological Society London Special Publications*, *268*(1), 1-23.

Green, P., Duddy, I., Laslett, G., Hegarty, K., Gleadow, A., Lovering, J.F. (1989), Thermal annealing of fission tracks in apatite 4. Quantitative modelling techniques and extension to geological timescales, *Chemical Geology*, 79, 155–182.

Grujic, D., M. Casey, C. Davidson, L. S. Hollister, R. Kündig, T. Pavlis, and S. Schmid (1996), Ductile extrusion of the Higher Himalayan Crystalline in Bhutan: evidence from quartz microfabrics, *Tectonophysics*, *260*, 21-43.

Grujic, D., C. J. Warren, and J. L. Wooden (2011), Rapid synconvergent exhumation of Miocene-aged lower orogenic crust in the eastern Himalaya, *Lithosphere*, *3*(5), 346-366.

Grujic D., K. T. Ashley, M. A. Coble, I. Coutand, D. A. Kellett, and N. Whynot (2016), Peak metamorphic and deformational temperatures across the Lesser Himalayan Sequence, Goldschmidt conference, Yokohama, Japan, 26 June-1 July 2016, Gold2016:abs:869.

Gupta, S. (1997), Himalayan drainage patterns and the origin of fluvial megafans in the Ganges foreland basin, *Geology*, *25*(1), 11-14.

Hammer, P., T. Berthet, G. Hetényi, R. Cattin, D. Drukpa, J. Chophel, S. Lechmann, N. Le Moigne, C. Champollion, and E. Doerflinger (2013), Flexure of the India plate underneath the Bhutan Himalaya, *Geophysical Research Letters*, *40*, 4225-4230.

Harris, N. B. W., M. Caddick, J. Kosler, S. Goswami, D. Vance, and A. G. Tindle (2004), The pressure-temperature-time path of migmatites from the Sikkim Himalaya, *Journal of Metamorphic Geology*, *22*(3), 249-264.

Harrison, T., F. Ryerson, P. Le Fort, A. Yin, O. Lovera, and E. Catlos (1997), A late Miocene-Pliocene origin for the central himalayan inverted metamorphism, *Earth and Planetary Science Letters*, *146*, E1-E8.

Hauck, M. L., K. D. Nelson, L. D. Brown, W. Zhao, and A. R. Ross (1998), Crustal structure of the Himalayan orogen at~ 90 east longitude from Project INDEPTH deep reflection profiles, *Tectonics*, *17*(4), 481-500.

He, D., A. A. G. Webb, K. P. Larson, A. J. Martin, and A. K. Schmitt (2015), Extrusion vs. duplexing models of Himalayan mountain building 3: duplexing dominates from the Oligocene to Present, *International Geology Review*, *57*(1), 1-27.

Herman, A., D. Seward, P. Valla, A. Carter, B. Kohn, S. Willett, and T. Ehlers (2013), Worldwide acceleration of mountain erosion under a cooling climate, *Nature*, *504*, doi:doi:10.1038.

Herman, F., J. Braun, and W. J. Dunlap (2007), Tectonomorphic scenarios in the Southern Alps of New Zealand, *Journal of Geophysical Research*, *112*, B04201, doi:10.1029/2004JB003472.

Herman, F., et al. (2010), Exhumation, crustal deformation, and thermal structure of the Nepal Himalaya derived from the inversion of thermochronological and thermobarometric data and modeling of the topography, *Journal of Geophysical Research*, *115*(B6), B06407.

Hodges, K. (2000), Tectonics of the Himalaya and southern Tibet from two perspectives, *Bulletin of the Geological Society of America*, *112*(3), 324-350.

Hodges, K. V., C. Wobus, K. Ruhl, T. Schildgen, and K. Whipple (2004), Quaternary deformation, river steepening, and heavy precipitation at the front of the Higher Himalayan Ranges, *Earth and Planetary Science Letters*, *220*, 379-389.

Kellett, D., D. Grujic, C. Mottram, and M. Mukul (2014), Virtual field guide for the Darjeeling-Sikkim Himalaya, India, in *Geological field trips in the Himalaya, Karakoram and Tibet*, edited by C. Montomoli, R. Carosi, R. Law, S. Singh and S. Rai, p. Paper 5, *Journal of the Virtual Explorer*, Electronic Edition.

Kellett, D. A., and D. Grujic (2012), New insight into the South Tibetan detachment system: Not a single progressive deformation, *Tectonics*, *31*(2), TC2007.

Kellett, D. A., D. Grujic, I. Coutand, J. Cottle, and M. Mukul (2013), The South Tibetan detachment system facilitates ultra rapid cooling of granulite-facies rocks in Sikkim Himalaya, *Tectonics*, *32*, 252-270.

Kumar, M., P. Hazarika, G. Prasad, A. Singh, and S. Saha (2012), Tectonic implications of the September 2011 Sikkim earthquake, *Current Science*, *102*, 788-792.

Lavé, J., and J.-P. Avouac (2000), Active folding of fluvial terraces across the Siwaliks Hills, Himalayas of central Nepal, *Journal of Geophysical Research*, *105*(B3), 5735-5770.

Long, S., N. McQuarrie, T. Tobgay, and D. Grujic (2011a), Geometry and crustal shortening of the Himalayan fold-thrust belt, eastern and central Bhutan, *Geological Society of America Bulletin*, *123*(7/8), 1427-1447.

Long, S., N. McQuarrie, T. Tobgay, D. Grujic, and L. Hollister (2011b), Geologic Map of Bhutan, *Journal of Maps*, *7*(1), 184-192.

Loveless, J. P., and B. J. Meade (2011), Partitioning of localized and diffuse deformation in the Tibetan Plateau from joint inversions of geologic and geodetic observations, *Earth and Planetary Science Letters*, *303*(1-2), 11-24.

Mancktelow, N. S., and B. Grasemann (1997), Time-dependent effects of heat advection and topography on cooling histories during erosion, *Tectonophysics*, *270*(3), 167-195.

McQuarrie, N., and T. Ehlers (2015), Influence of thrust belt geometry and shortening rate on thermochronometer cooling ages: Insights from thermokinematic and erosion modeling of the Bhutan Himalaya, *Tectonics*, doi:10.1002/2014TC003783.

McQuarrie, N., D. Robinson, S. Long, T. Tobgay, D. Grujic, G. Gehrels, and M. Ducea (2008), Preliminary stratigraphic and structural architecture of Bhutan: Implications for the along strike architecture of the Himalayan system, *Earth and Planetary Science Letters*, *272*(1), 105-117.

Meigs, A. J., D. W. Burbank, and R. A. Beck (1995), Middle-late Miocene (>10 Ma) formation of the Main Boundary thrust in the western Himalaya, *Geology*, *23*(5), 423-426.

Mitra, G., K. Bhattacharyya, and M. Mukul (2010), The Lesser Himalayan duplex in Sikkim: Implications for variations in Himalayan shortening, *Journal of the Geological Society of India*, *75*(1), 289-301.

Mohan, A., B. Windley, and M. Searle (1989), Geothermobarometry and development of inverted metamorphism in the Darjeeling-Sikkim region of the eastern Himalaya, *Journal of Metamorphic Geology*, *7*, 95-110.

Mottram, C. (2014), Crustal extrusion along the Main Central Thrust in the Sikkim Himalaya, Unpublished Thesis.

Mottram, C., T. Argles, N. Harris, R. Parrish, M. Horstwood, C. Warren, and S. Gupta (2014a), Tectonic interleaving along the Main Central Thrust, Sikkim Himalaya, *Journal of the Geological Society of London*, *171*, 255-268.

Mottram, C., C. Warren, D. Regis, N. Roberts, N. Harris, T. Argles, and R. Parrish (2014b), Developing an inverted Barrovian sequence; insights from monazite petrochronology, *Earth and Planetary Science Letters*, *403*, 418-431.

Mottram, C., R. Parrish, D. Regis, C. Warren, T. Argles, and N. Harris (2015), Using U-Th-Pb petrochronology to determine rates of ductile thrusting: time windows into the Main Central Thrust, Sikkim Himalaya, *Tectonics*, doi:10.1002/2014TC003743.

Mukul, M. (2000), The geometry and kinematics of the Main Boundary Thrust and related neotectonics in the Darjiling Himalayan fold-and-thrust belt, West Bengal, India, *Journal of Structural Geology*, *22*(9), 1261-1283.

Mukul, M. (2010), First-order kinematics of wedge-scale active Himalayan deformation: Insights from the Darjiling-Sikkim-Tibet (DaSiT) wedge, *Journal of Asian Earth Sciences*, *39*, 645-657.

Mukul, M., S. Jade, A. K. Bhattacharyya, and K. Bhusan (2010), Crustal shortening in convergent orogens: Insights from global positioning system (GPS) measurements in northeast India, *Journal of the Geological Society of India*, *75*(1), 302-312.

Mukul, M., M. Jaiswal, and A. K. Singhvi (2007), Timing of recent out-of-sequence active deformation in the frontal Himalayan wedge: Insights from the Darjiling sub-Himalaya, India, *Geology*, *35*(11), 999-1002.

Nábělek, J., G. Hetényi, J. Vergne, S. Sapkota, B. Kafle, M. Jiang, H. Su, J. Chen, B.-S. Huang, and H.-C. Team (2009), Underplating in the Himalaya-Tibet collision zone revealed by the Hi-CLIMB experiment, *Science*, *325*(5946), 1371-1374.

Naito, N., Y. Ageta, S. Iwata, Y. Matsuda, R. Suzuki, Karma, and H. Yabuki (2006), Glacier shrinkages and climate conditions around Jichu Dramo Glacier in the Bhutan Himalayas from 1998 to 2003, *Bulletin of glaciological Research*, *23*, 51-61.

Najman, Y., E. Appel, M. Boudagher- Fadel, P. Bown, A. Carter, E. Garzanti, L. Godin, J. Han, U. Liebke, and G. Oliver (2010), Timing of India- Asia collision: Geological, biostratigraphic, and palaeomagnetic constraints, *Journal of Geophysical Research*, *115*(B12).

Najman, Y., L. Bracciali, R. Parrish, E. Chisty, and A. Copley (2016), Evolving strain partitioning in the Eastern Himalaya: The growth of the Shillong Plateau, *Earth and Planetary Science Letters*, *433*, 1-9.

Nelson, K. D., et al. (1996), Partially molten middle crust beneath southern Tibet: Synthesis of project INDEPTH results, *Science*, *274*, 1684-1688.

Neogi, S., S. Dasgupta, and M. Fukuoka (1998), High P-T polymetamorphism, dehydration melting, and generation of migmatites and granites in the Higher Himalayan Complex, Sikkim, India, *Journal of Petrology*, *39*(1), 61-99.

Pradhan, R., S. Prajapati, S. Chopra, and A. Kumar (2013), Causative source of Mw. 6.9 Sikkim-Nepal border earthquake of September 2011: GPS baseline observations and strain analysis, *Journal of Asian Earth Sciences*, *70-71*, 179-192.

Priestley, K., J. Jackson, D. McKenzie (2008), Lithospheric structure and deep earthquakes beneath India, the Himalaya and southern Tibet, *Geophysical Journal International*, 172(1), 345-362.

Rao, R. U. M., G. V. Rao, and H. Narain (1976), Radioactive heat generation and heat flow in the Indian shield, *Earth and Planetary Science Letters*, 30(1), 57-64.

Reiners, P. W. (2005), Zircon (U-Th)/He thermochronometry, *Reviews in Mineralogy and Geochemistry*, *58*(1), 151-179.

Rickwood, P., and M. Sambridge (2006), Efficient parallel inversion using the Neighborhood Algorithm, *Geochemistry Geophysics Geosystems*, *7*(11), doi:10.1029/2006GC001246.

Robert, X., P. van der Beek, J. Braun, C. Perry, M. Dubille, and J.-L. Mugnier (2009), Assessing Quaternary reactivation of the Main Central thrust zone (central Nepal Himalaya): New thermochronologic data and numerical modeling, *Geology*, *37*(8), 731-734, doi:10.1130/G25736A.1.

Robert, X., P. Van Der Beek, J. Braun, C. Perry, and J.-L. Mugnier (2011), Control of detachment geometry on lateral variations in exhumation rates in the Himalaya: Insights from low-temperature thermochronology and numerical modeling, *Journal of Geophysical Research*, *116*(B5), B05202.

Robinson, D., P. DeCelles, P. Patchett, and C. Garzione (2001), The kinematic evolution of the Nepalese Himalaya interpreted from Nd isotopes, *Earth and Planetary Science Letters*, *192*, 507-521.

Robinson, D., and A. Martin (2014), Reconstructing the Greater Indian margin: A balanced cross section in central Nepal focusing on the Lesser Himalayan duplex, *Tectonics*, *33*(11), 2143-2168.

Roy S., and R. U. M. Rao (2000), Heat flow in the Indian shield, *Journal of Geophysical Research: Solid Earth*, 105(B11), 25587-25604.

Rubatto, D. S., S. Chakraborty, and S. Dasgupta (2013), Timescales of crustal melting in the Higher Himalayan Crystallines (Sikkim, Eastern Himalaya) inferred from trace element-constrained monazite and zircon chronology, *Contributions to Mineralogy and Petrology*, *165*, 349-372.

Sambridge, M. (1999a), Geophysical inversion with a Neighborhood algorithm -I. Searching a parameter space, *Geophysical Journal International*, *138*, 479-494.

Sambridge, M. (1999b), Geophysical inversion with a Neighborhood algorithm—II. Appraising the ensemble, *138*(3), 727-746.

Schelling, D., and K. Arita (1991), Thrust tectonics, crustal shortening, and the structure of the far-eastern Nepal Himalaya, *Tectonics*, *10*(5), 851-862.

Schopf, J., V. Tewari, and A. Kudryavtsev (2008), Discovery of a new chert-permineralized microbiota in the Proterozoic Buxa Formation of the Ranjit window, Sikkim, northeast India, and its astrobiological implications, *Astrobiology*, *8*(4), 735-746.

Schwan, W. (1980), *Shortening structures in Eastern and Northwestern Himalayan rocks*, Today and Tomorrow's Printers and Publishers, New Delhi.

Shuster, D., T. Ehlers, M. Rusmoren, and K. Farley (2005), Rapid Glacial Erosion at 1.8 Ma Revealed by $^{4}He/^{3}He$ Thermochronometry, *Science*, *310*, 1668-1670.

Singer, J., E. Kissling, T. Diehl and G. Hetényi (2015), Evidence for along-strike variations in the crustal deformation beneath the Bhutan Himalaya from receiver function imaging and seismicity, AGU Fall Meeting, San Francisco 14-18 December 2015, T13G-10.

Srivastava, P., and G. Mitra (1994), Thrust geometries and deep structure of the outer and lesser Himalaya, Kumaon and Garhwal (India): Implications for evolution of the Himalayan fold-and-thrust belt, *Tectonics*, *13*(1), 89-109.

Stüwe, K., and M. Hintermüller (2000), Topography and isotherms revisited: the influence of laterally migrating drainage divides, *Earth and Planetary Science Letters*, *184*(1), 287-303.

Stüwe, K., L. White, and R. Brown (1994), The influence of eroding topography on steady-state isotherms. application to fission track analysis, *Earth and Planetary Science Letters*, *124*(1-4), 63-74.

Suppe, J. (1983), Geometry and kinematics of fault-bend folding, *American Journal of Science*, *283*(7), 684-721.

Thiede, R., and T. Ehlers (2013), Large spatial and temporal variations in Himalayan denudation, *Earth and Planetary Science Letters*, *371-372*, 278-293.

Thomson, S. N., M. T. Brandon, J. H. Tomkin, P. W. Reiners, C. Vasquez, and N. J. Wilson (2010), Glaciation as a destructive and constructive control on mountain building, *Nature 467*, 313-317.

Tiwari, V., M. Vyghreswara Rao, D. Mishra, and B. Singh (2006), Crustal structure across Sikkim, NE Himalaya from new gravity and magnetic data, *Earth and Planetary Science Letters*, *247*(1), 61-69.

Valla, P., F. Herman, P. A. van der Beek, and J. Braun (2010), Inversion of thermochronological age-elevation profiles to extract independent estimates of denudation and relief history--I: Theory and conceptual model, *Earth and Planetary Science Letters*, *295*, 511-522.

van der Beek, P., X. Robert, J. Mugnier, M. Bernet, P. Huyghe, and E. Labrin (2006), Late Miocene - Recent exhumation of the central Himalaya and recycling in the foreland basin assessed by apatite fission-track thermochronology of Siwalik sediments, Nepal, *Basin Research*, *18*(4), 413-434.

Vernant, P., R. Bilham, W. Szeliga, D. Drukpa, S. Kalita, A. Bhattacharya, V. Gaur, P. Pelgay, R. Cattin, and T. Berthet (2014), Clockwise rotation of the Brahmaputra Valley relative to India: Tectonic convergence in the eastern Himalaya, Naga Hills, and Shillong Plateau, *Journal of Geophysical Research 119*, 6558-6571.

von Loczy, L. (1907), Beobachtungen im östlichen Himalaya, *Földr*. *Közlem*, *35*(117).

Whipp, D. M., and T. A. Ehlers (2007), Influence of groundwater flow on thermochronometer-derived exhumation rates in the central Nepalese Himalaya, *Geology*, *35*(9), 851-854.

Whipp, D. M., T. A. Ehlers, J. Braun, and C. D. Spath (2009), Effects of exhumation kinematics and topographic evolution on detrital thermochronometer data, *Journal of Geophysical Research*, *114*, F04021.

Whipp Jr., D. M., T. A. Ehlers, A. E. Blythe, K. W. Huntington, K. V. Hodges, and D. W. Burbank (2007), Plio-Quaternary exhumation history of the central Nepalese Himalaya: 2. Thermokinematic and thermochronometer age prediction model, *Tectonics*, *26*, TC3003.

Whipple, K. (2014), Can erosion drive tectonics?, *Science*, *346*, 918-919.

Whipple, K. X. (2009), The influence of climate on the tectonic evolution of mountain belts, *Nature Geosciences*, *2*(2), 97-104.

Wobus, C., A. Heimsath, K. Whipple, and K. Hodges (2005), Active out-of-sequence thrust faulting in the central Nepalese Himalaya, *Nature*, *434*, 1008-1011.

Wolf, R, K. Farley, and D. M. Kass (1998), Modeling of the temperature sensitivity of the apatite (U-Th)/He thermochronometer, *Computational Geosciences*, 148, 105-114.

Woodward, N., S. Boyer, and J. Suppe (1989), *Balanced Geological Cross Section: an Essential Technique in Geological Research and Exploration American Geophysical Union*, American Geophysical Union, Washington, DC.

Yin, A. (2006), Cenozoic tectonic evolution of the Himalayan Orogen as constrained by along-strike variation of structural geometry, exhumation history, and foreland sedimentation, *Earth-Science Reviews*, *76*(1-2), 1-131.

Zahid, K., and A, Uddin, 2005, Influence of overpressure on formation velocity evaluation of Neogene strata from the eastern Bengal Basin, Bangladesh, *Journal of Asian Earth Sciences*, 25(3), 419-429.

Zhuang, G., Y. Najman, S. Guillot, M. Roddaz, P.-O. Antoine, G. Métais, A. Carter, L. Marivaux, and S. Solangi (2015), Constraints on the collision and the pre-collision tectonic configuration between India and Asia from detrital geochronology, thermochronology, and geochemistry studies in the lower Indus basin, Pakistan, *Earth and Planetary Science Letters*, *432*, 363-373.

Figure 1. Geological map of the Eastern Himalaya (Modified after *Grujic et al*., [2011] and *Kellett et al*., [2014]). Dark grey frame on map in inset shows location of Figure 1. Abbreviations are: MFT, Main Frontal Thrust; MBT, Main Boundary Thrust; RT, Ramgarh Thrust; MCT, Main Central Thrust; STDS, South Tibetan Detachment System. Pale blue (pink) dots (and adjoined numbers) are AFT (ZHe) sample location from this study (also reported in Table 1 with "ISIK" prefix); pale blue squares indicate AFT sample locations from *Kellett et al*., [2013]. Lines A-A' and B-B' indicate cross-section location presented in Figure 2.

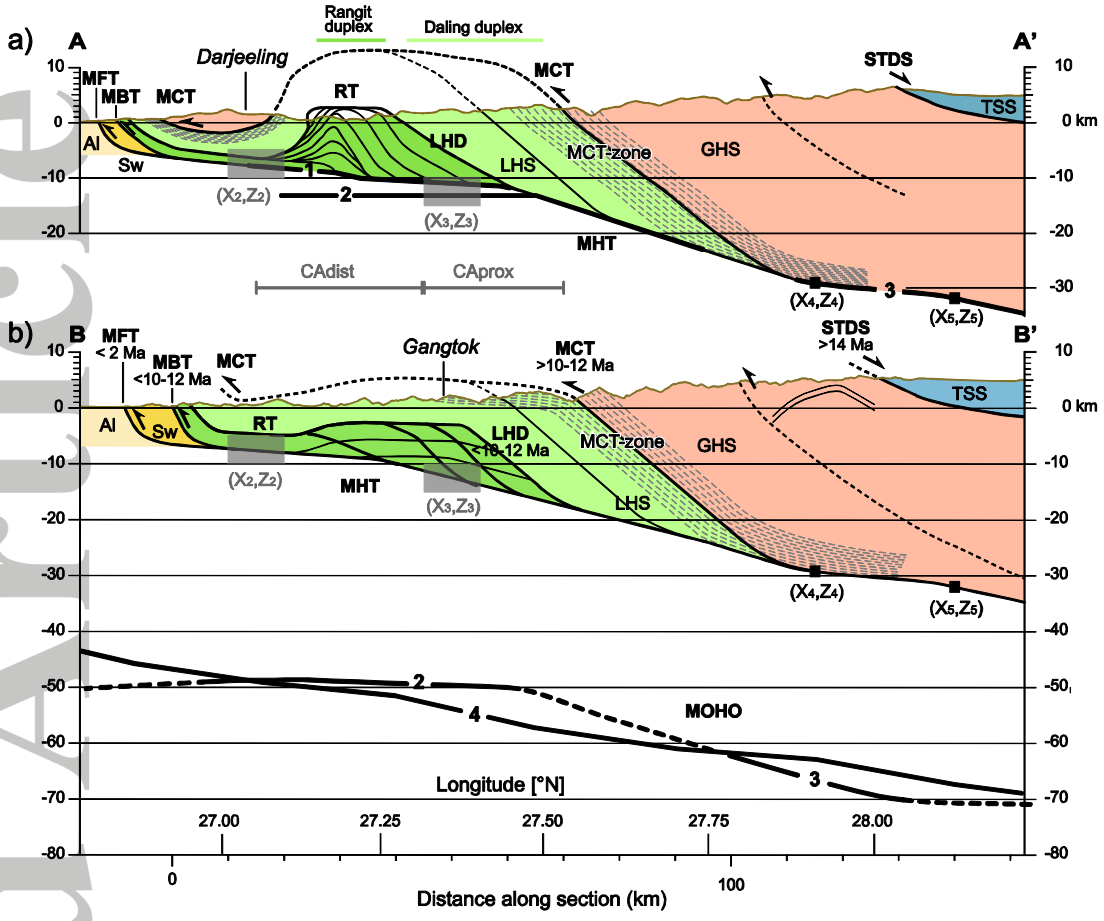

Figure 2. NNE-SSW geological cross-sections across West Bengal and Sikkim (redrawn after *Kellett et al*., [2013]; *Kellett et al*., [2014] and *Bhattacharyya and Mitra*, [2009]. For location, see lines A-A' and B-B' in Figure 1. Ages indicate the onset (<) or termination (>) of ductile shearing and brittle faulting on the main structures. Abbreviations are: TSS, Tethyan Sedimentary Sequence; GHS, Greater Himalayan Sequence; LHD, Lesser Himalayan Duplex; LHS, Lesser Himalayan Sequence; Sw, Siwaliks sediments; Al, Alluvium; MHT, Main Himalayan Thrust. Abbreviations of other structures are as in Figure 1. Geological and geophysical constraints on the MHT and the Moho geometries are represented by the numbered black and grey bold lines with 1. *Bhattacharyya and Mitra*, [2009]; 2. *Acton et al*., [2011]; 3. *Hauck et al*., [1998] (INDEPTH I) and 4. [Hetényi, 2007 #1282]. Black squares are geometric constraints from INDEPTH I. Grey rectangles and horizontal bars represent the geometric parameters that are investigated in our inversions (see text for explanations).

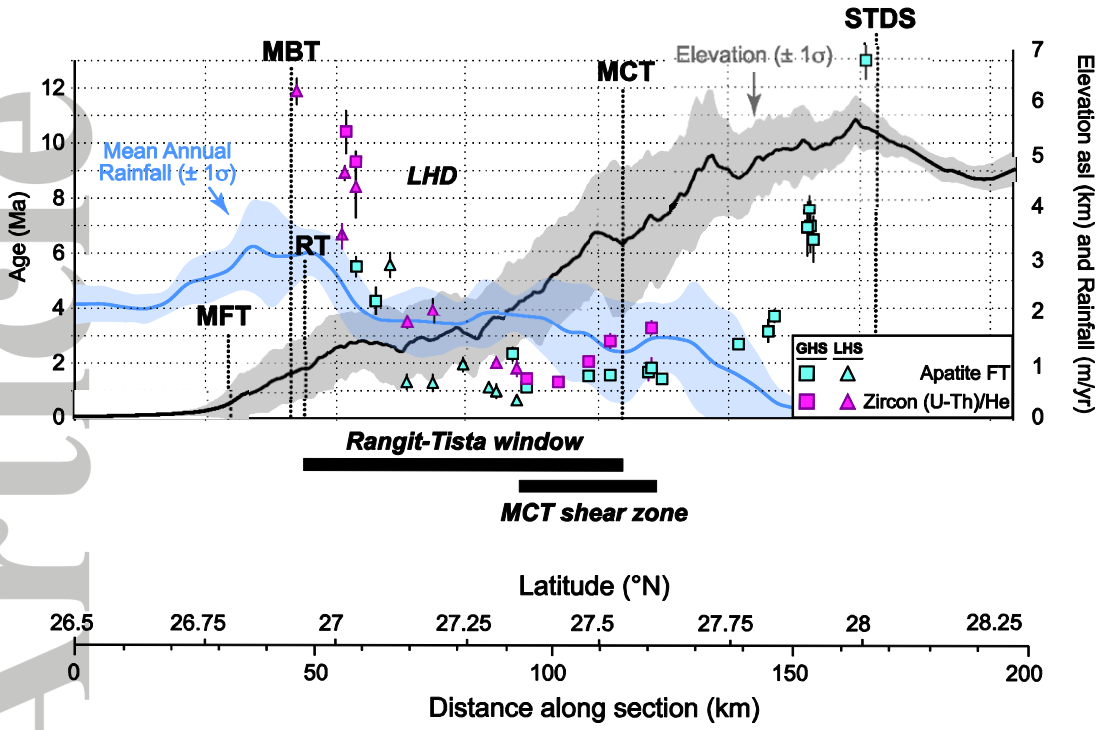

Figure 3. Spatial distribution of cooling ages across the Sikkim Himalaya. Each sample location is projected perpendicularly to cross-section line BB' (Figure 1) and plotted against latitude (or horizontal distance) along this line. Cooling age data are represented by squares (triangles) when the samples are derived from the GHS (LHS). Mean topographic profile is represented by the bold black line and standard deviation by the shaded gray area. Mean annual rainfall distribution is represented by the bold blue line and standard deviation by the blue shaded area and taken from *Bookhagen and Burbank*, 2010. The location of the main shear zones is represented by vertical dotted lines. Abbreviations are as in Figures 1 and 2.

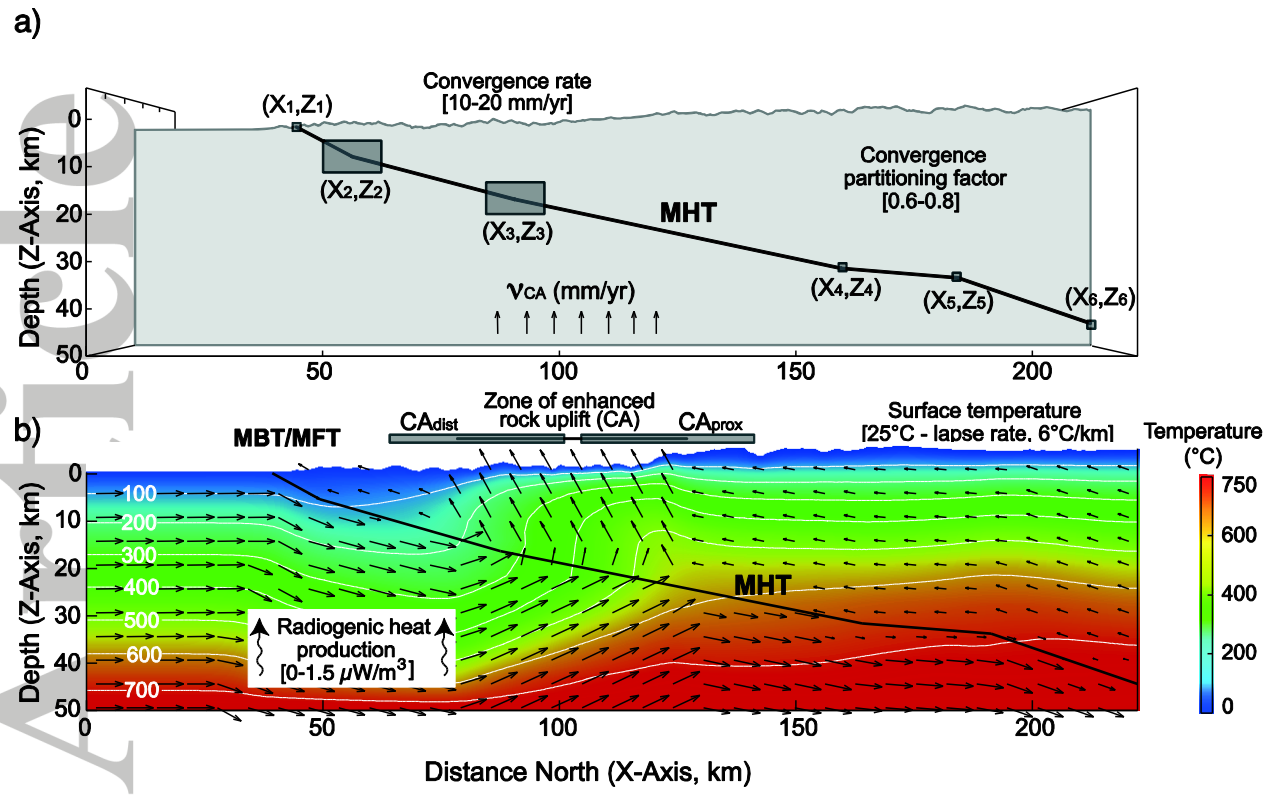

Figure 4. Thermokinematic model boundary conditions, free parameters, and example thermal solution. (a) The kinematic model has Indo-Tibetan convergence partitioned on either side of the MHT, which is defined by a series of points along its length that may occupy any position within each search box. (b) Isotherms (thin white lines) show significant perturbations to the subsurface thermal field, mainly from advection using the velocity field (black arrows) generated by the kinematic model. Enhanced rock uplift simulates vertical crustal accretion (or thickening) (CA) resulting from duplex structural development.

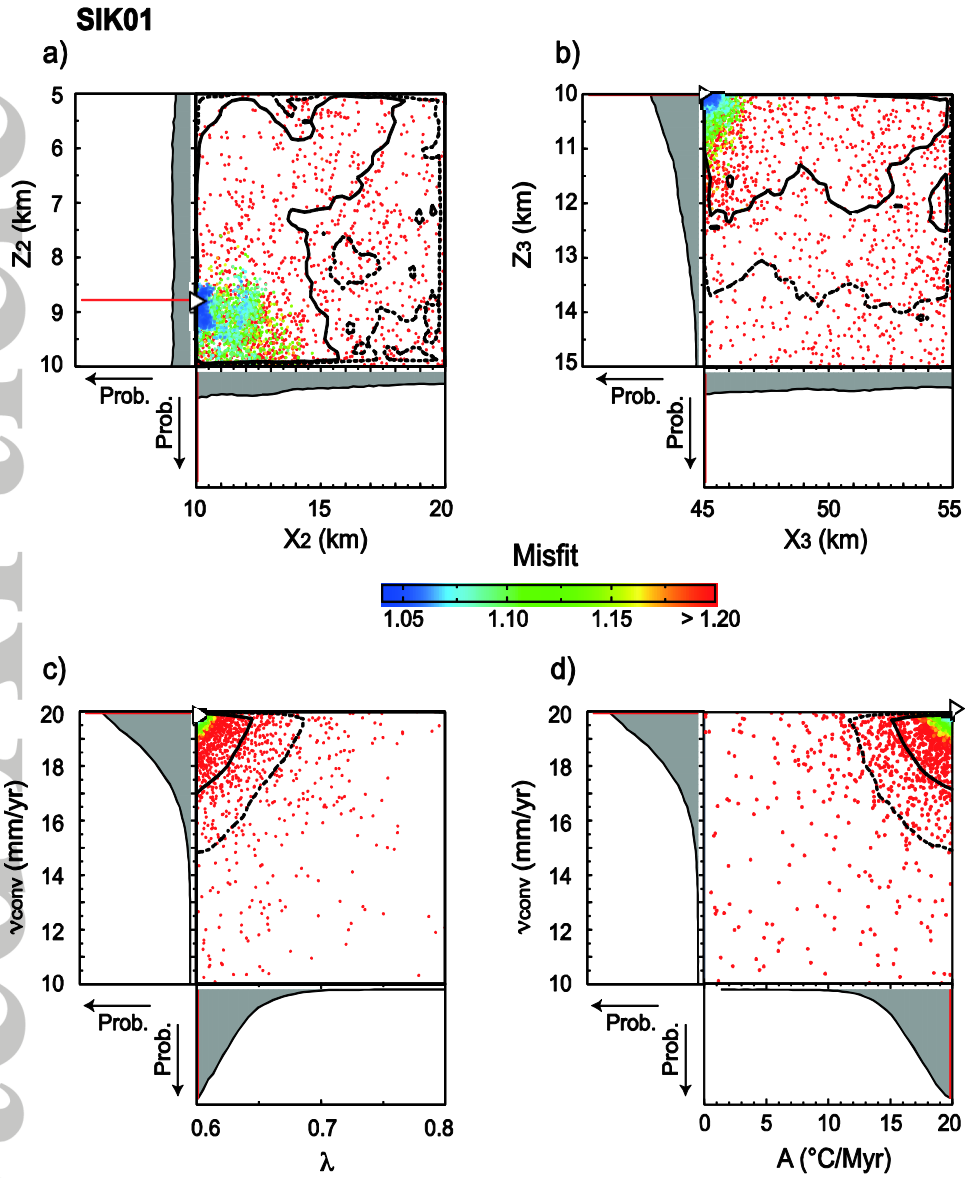

Figure 5. Inversion results for model SIK01 solving for 7 free parameters (see Table 5). Each dot represents a single forward model, and its color corresponds to the goodness of fit to the data (red (blue) dot = highest (lowest) misfit). The white triangle represents the parameter values obtained from the forward model with the lowest misfit. One-dimensional Posterior Probability Density Functions (1D PPDFs) derived from the NA appraisal are shown adjacent to the axes for each parameter. The red lines indicate parameter values for the lowest misfit forward model. Two-dimensional PPDFs (2D PPDFs) are represented by lines overlying the scatter diagram where the solid black line is the 1σ confidence interval and the dashed line the 2σ confidence interval.

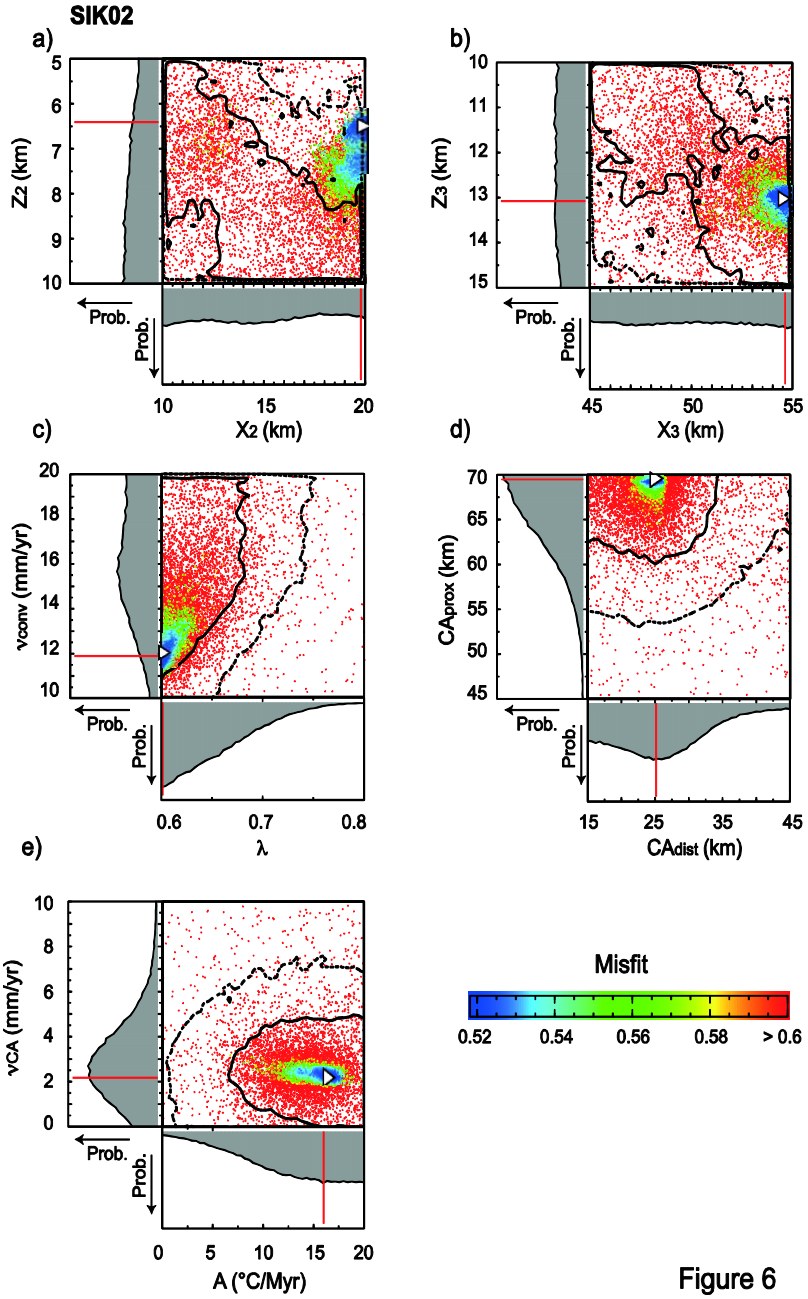

Figure 6. Inversion results for model SIK02 solving for 10 parameters (see Table 5). Symbols are same as for Figure 5.

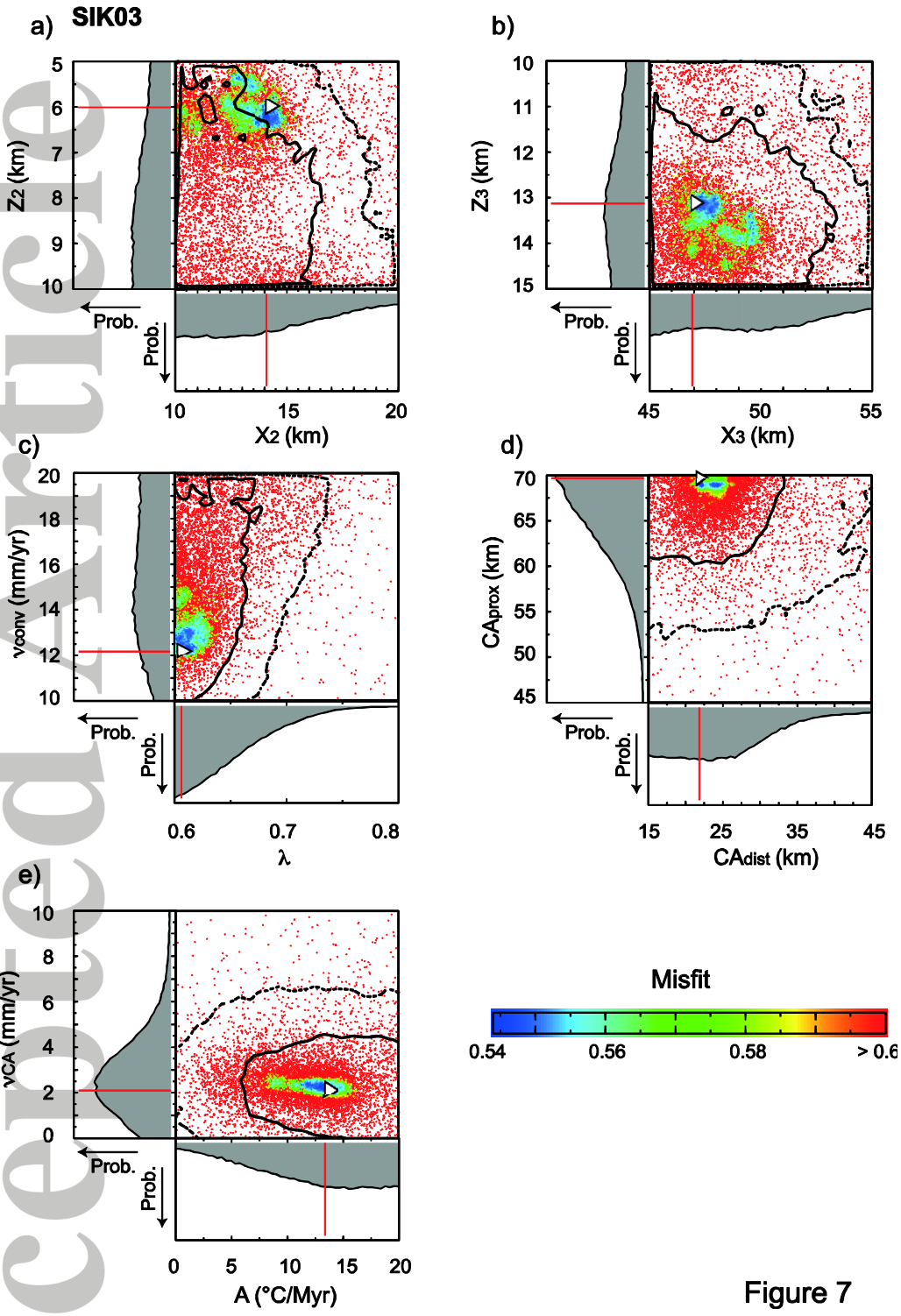

Figure 7

Figure 7. Inversion results for model SIK03 solving for 10 parameters (see Table 5).

Symbols are same as for Figure 5.

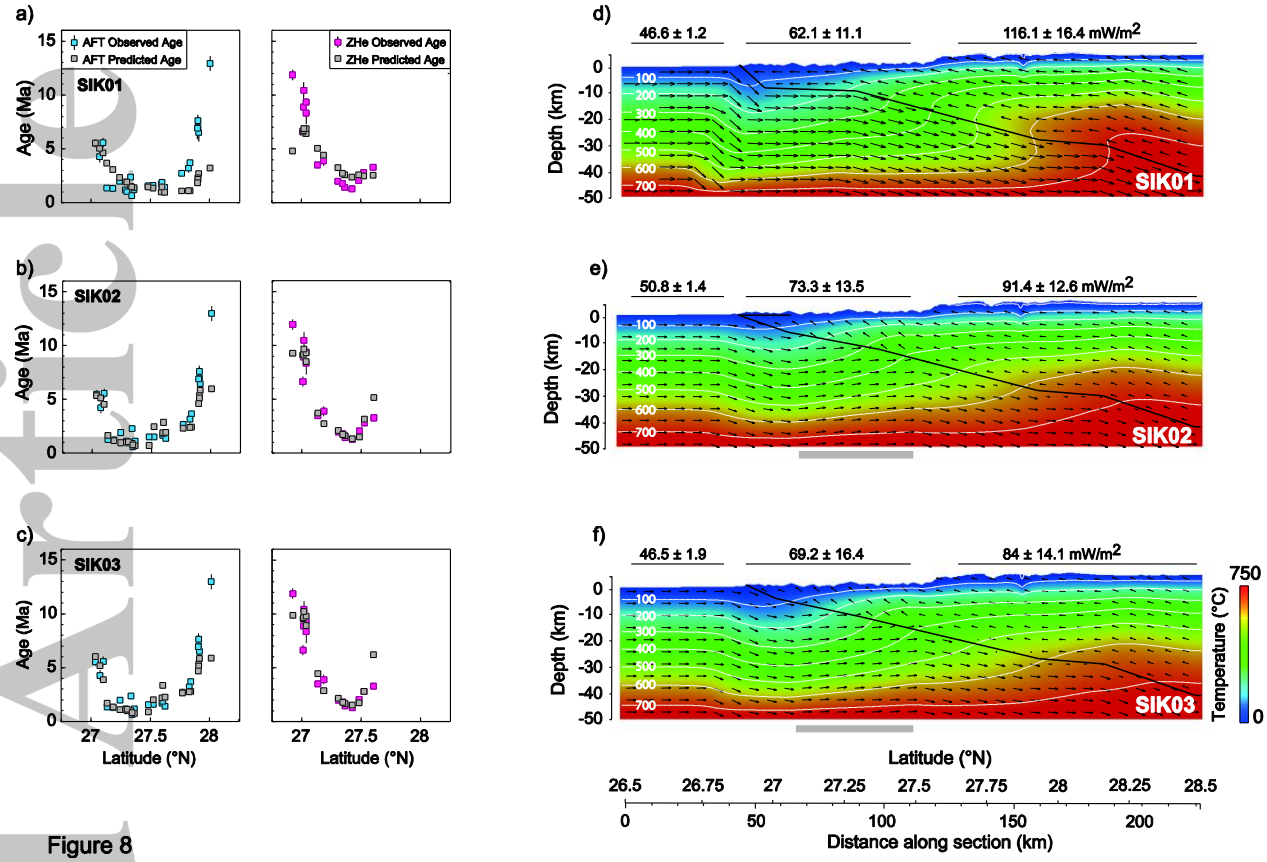

Figure 8

Figure 8. Predicted versus observed cooling ages from models at steady-state topography SIK01 and SIK02 (a & b) and evolving topography SIK03 (c). (e-f) Thermal, velocity fields (black arrows) and MHT geometry obtained from inversions SIK01, SIK02 and SIK03. The grey bars indicate the location of crustal accretion.

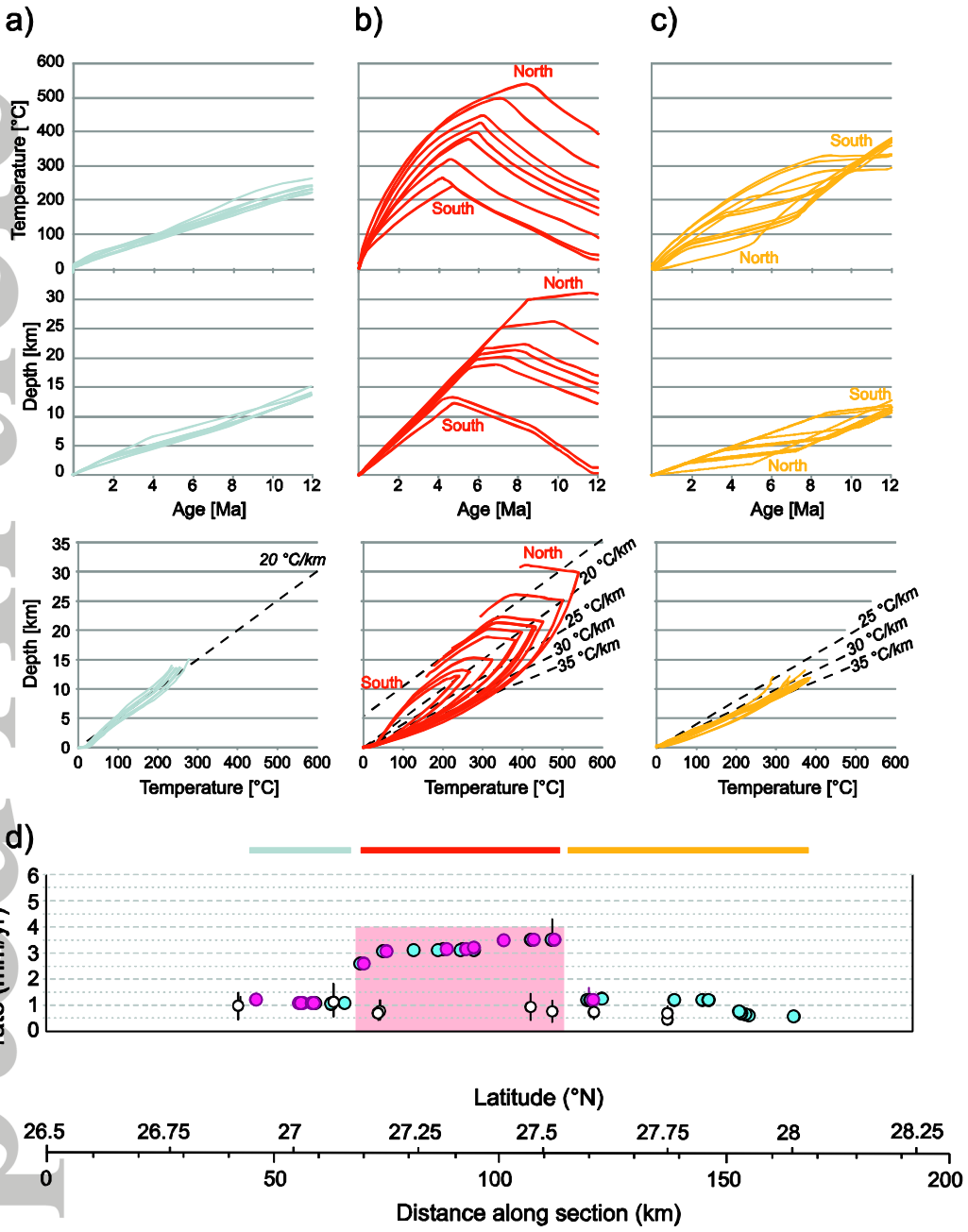

Figure 9. Long-term exhumation rates and t-T-D paths. (a-c) time-Temperature-Depth trajectories for samples located south of the duplex (grey lines), in the duplex (red lines) and north of it (yellow lines). d) Distribution of long-term exhumation rates averaged for the preferred tectonomorphic model for the Sikkim Himalaya (SIK02). Pale blue (pink) dots are values obtained from AFT (ZHe) data and white circles are values obtained from detrital AFT thermochronology by *Abrahami et al.*, [2016]. The pink zone indicates the location of enhanced rock uplift at the end of run SIK02.

Table 1. Samples identification and location

Sample	Unit	Longitude (°E)	Latitude (°N)	Elev. (m)	AFT	ZHe
ISIK05	Gondwana Fm. (Quartzite)	88.4548	26.9243	181	x	1
ISIK07	Daling Fm. (Schist w. quartz)	88.4268	27.0380	215	x	1
ISIK08	Daling Fm. (Schist w. quartz)	88.4252	27.0103	794	x	1
ISIK09	Daling/Reyang Fm. (Quartzite & schist)	88.3726	27.0159	1162	x	1
ISIK10	GHS Fm. (Migmatite gneiss)	88.3458	27.0380	1729	1	1
ISIK11	GHS Fm. (Migmatite gneiss)	88.3021	27.0183	2088	x	1
ISIK12	Daling Fm.(?) (Mylonitic granite)	88.5507	27.1022	1540	1	x
ISIK13	GHS Fm. (Migmatite)	88.6655	27.0745	1939	1	x
ISIK14	Daling Fm. (Schist & quartzite)	88.5226	27.2424	458	1	x
ISIK20	GHS Fm. (?) (Migmatite orthogneiss)	88.6271	27.3369	1846	1	x
ISIK24	GHS Fm. (Pegmatite)	88.6488	27.5961	1676	1	x
ISIK25	GHS Fm. (Leucogranite)	88.6186	27.6237	1812	1	x
ISIK27	GHS Fm. (Leucogranite)	88.5507	27.8385	3641	1	x
ISIK28	GHS Fm. (Migmatite)	88.5480	27.8256	3400	1	x
ISIK29	GHS Fm. (Quartzite)	88.5418	27.7689	3166	1	x
ISIK33	Daling/Reyang Fm. (Quartzite)	88.3946	27.2911	1493	1	x
ISIK34	Daling Fm. (Quartzite & schist)	88.3677	27.3055	1923	1	1
ISIK36	Gondwana Fm. (Black slate)	88.2795	27.1350	326	1	1
ISIK37	Gondwana Fm. (Black slate)	88.3171	27.1848	457	1	1
ISIK38	GHS Fm. (Pegmatite)	88.1840	27.5244	3978	1	1
ISIK39	GHS Fm. (Augengneiss)	88.1878	27.6030	4909	1	1
ISIK41	GHS Fm. (Leucogranite)	88.1791	27.4822	3761	1	1
ISIK42	GHS Fm. (Migmatite)	88.1913	27.4246	2237	x	1
ISIK44	GHS Fm. (Migmatite gneiss)	88.2244	27.3640	1571	1	1
ISIK45	Daling Fm. (Sandstone)	88.2628	27.3450	1509	1	1
SK55	GHS Fm. (Leucogranite)	88.7069	28.0098	5282	2	x
SK69	GHS Fm. (Gneiss)	88.5366	27.9119	4754	2	x
SK70	GHS Fm. (Migmatite gneiss)	88.5361	27.9066	4485	2	x
SK71	GHS Fm. (Migmatite gneiss)	88.5369	27.9046	4352	2	x
SK72	GHS Fm. (Leucogranite)	88.5384	27.9010	4131	2	x

Notes: x: no analysis available; 1: this study; 2: Kellett et al., 2013.

Table 2. Apatite fission-track results

Sample	Number of grains	Spontaneous Track Density $\rho s \times 10^6$ cm^{-2} (Ns)	Induced Track Density $\rho i \times 10^6$ cm^{-2} (Ni)	Dosimeter Track Density $\rho d \times 10^6$ cm^{-2} (Nd)	$P(\chi^2)$ (%)	Central Age ± 1σ (Ma)	U (ppm)	Dpars (μm)	Dpars STD (μm)
ISIK10	20	0.1525 (241)	4.1538 (6565)	0.80947 (3266)	84.1	5.5 ± 0.4	69	2.09	0.87
ISIK12	18	0.1359 (172)	3.7233 (4711)	0.82234 (3266)	63.7	5.6 ± 0.5	60	2.23	0.91
ISIK13	19	0.0473 (71)	1.7111 (2566)	0.82878 (3266)	94.3	4.2 ± 0.5	26	1.96	0.84
ISIK14	20	0.0395 (60)	3.1348 (4763)	0.83522 (3266)	92.8	1.9 ± 0.3	51	2.09	0.86
ISIK20	20	0.0422 (72)	2.9276 (4995)	0.87384 (3266)	89.8	2.3 ± 0.3	44	1.94	0.94
ISIK24	20	0.0158 (27)	1.5578 (2658)	0.89959 (3266)	96.4	1.7 ± 0.3	22	1.99	0.92
ISIK25	20	0.0198 (34)	2.3653 (4057)	0.90602 (3266)	87.4	1.4 ± 0.2	35	2.09	0.93
ISIK27	17	0.1691 (249)	7.7157 (11363)	0.91246 (3266)	33.6	3.7 ± 0.2	111	2.18	0.89
ISIK28	17	0.0384 (58)	2.0575 (3104)	0.91890 (3266)	99.7	3.2 ± 0.4	29	2.14	0.99
ISIK29	17	0.0529 (77)	3.3531 (4878)	0.92534 (3266)	99.6	2.7 ± 0.3	47	2.17	1.05
ISIK33	17	0.0292 (44)	4.4265 (6678)	0.94465 (3266)	93.3	1.1 ± 0.2	62	2.05	0.94
ISIK34	15	0.0135 (17)	2.3976 (2956)	0.95108 (3266)	78.8	1.0 ± 0.2	32	2.14	0.97
ISIK36	17	0.0194 (26)	2.6118 (3497)	0.95752 (3266)	92.8	1.3 ± 0.3	35	2.26	0.98
ISIK37	12	0.0166 (17)	2.3151 (2370)	0.96396 (3266)	58.6	1.3 ± 0.3	31	2.09	1.10
ISIK38	19	0.0346 (59)	3.9878 (6804)	0.97039 (3266)	76.2	1.6 ± 0.2	54	2.01	0.92
ISIK39	17	0.0186 (27)	1.8113 (2635)	0.97683 (3266)	98.0	1.8 ± 0.4	28	2.09	0.97
ISIK41	19	0.0483 (82)	5.6811 (9052)	0.98327 (3266)	98.8	1.5 ± 0.2	76	2.16	1.03
ISIK44	13	0.0334 (27)	5.2339 (4230)	0.98971 (3266)	96.0	1.2 ± 0.2	69	2.27	1.10
ISIK45	18	0.047 (20)	4.4104 (6020)	0.99614 (3266)	52.5	0.6 ± 0.1	56	1.94	1.01

Abbreviations: N, number of individual grains dated per sample; ρ_S, spontaneous track density; Ns, number of spontaneous tracks counted in the sample; ρ_i, induced track density in external detector (muscovite); Ni, number of induced tracks counted in external detector; ρ_d, induced track density in external detector adjacent to CN_5 dosimetry glass; Nd, number of induced tracks in external detector adjacent to dosimeter; and $P(\chi^2)$, chi-square probability.

Table 3. Zircon (U-Th)/He results

Samples	^{4}He	^{238}U	^{235}Th	^{232}Th	Mean length	Mean radius	Raw age	Ft	Corrected age	Mean age	Age error (1σ)
	(Mol)	(Mol)	(Mol)	(Mol)	(μm)	(μm)	(Ma)		(Ma)	(Ma)	(Ma)
ISIK05-1	*6.95E-13*	*3.33E-11*	*2.41E-13*	*2.04E-12*	*213.57*	*98.11*	*15.93*	*0.76*	*20.30*	**11.87**	**0.49**
ISIK05-2	2.98E-13	2.59E-11	1.88E-13	1.93E-12	252.62	100.82	8.75	0.77	10.95		
ISIK05-3	3.57E-13	2.62E-11	1.90E-13	9.29E-12	250.31	77.41	9.76	0.72	13.02		
ISIK05-4	4.15E-13	3.55E-11	2.57E-13	1.27E-11	259.84	88.21	8.37	0.75	10.82		
ISIK05-5	2.75E-13	2.22E-11	1.61E-13	2.36E-12	189.21	75.62	9.39	0.70	12.67		
ISIK07-1	5.96E-14	6.55E-12	4.75E-14	6.63E-13	219.91	74.77	6.89	0.71	9.39	**8.33**	**1.05**
ISIK07-2	7.99E-14	6.67E-12	4.84E-14	8.83E-13	199.13	74.72	9.00	0.70	12.24		
ISIK07-3	4.99E-14	6.62E-12	4.80E-14	9.17E-13	207.26	66.62	5.66	0.68	7.92		
ISIK07-4	7.23E-14	1.12E-11	8.16E-14	9.24E-13	279.64	72.91	4.88	0.71	6.56		
ISIK07-5	6.85E-14	1.24E-11	8.98E-14	1.47E-12	244.36	80.13	4.17	0.73	5.52		
ISIK08-1	8.85E-14	1.57E-11	1.14E-13	1.94E-12	191.02	114.31	4.24	0.77	5.29	**6.62**	**0.48**
ISIK08-2	5.07E-14	6.16E-12	4.47E-14	3.10E-12	234.39	88.21	5.71	0.74	7.40		
ISIK08-3	1.04E-13	1.50E-11	1.09E-13	1.01E-11	233.49	89.11	4.65	0.75	6.03		
ISIK08-4	2.16E-14	2.62E-12	1.90E-14	9.28E-13	152.97	71.11	5.91	0.67	8.30		
ISIK08-5	2.98E-13	4.87E-11	3.53E-13	3.51E-12	202.75	87.31	4.66	0.73	6.10		
ISIK09-1	4.84E-14	5.76E-12	4.18E-14	1.09E-12	285.97	90.01	6.23	0.76	8.03	**8.89**	**0.25**
ISIK09-2	7.75E-14	8.87E-12	6.43E-14	6.15E-13	192.77	77.41	6.66	0.71	9.07		
ISIK09-3	7.37E-14	8.74E-12	6.34E-14	7.14E-13	173.80	65.72	6.41	0.67	9.18		
ISIK09-4	7.23E-14	8.22E-12	5.96E-14	8.42E-13	211.77	68.41	6.65	0.69	9.28		
ISIK09-5	*5.76E-14*	*2.31E-11*	*1.67E-13*	*3.35E-12*	*190.96*	*76.51*	*1.87*	*0.71*	*2.53*		
ISIK10-1	2.62E-13	3.20E-11	2.32E-13	2.21E-12	255.23	80.36	6.25	0.73	8.31	**9.34**	**0.36**
ISIK10-2	3.64E-13	3.95E-11	2.87E-13	3.82E-12	291.41	98.73	6.98	0.78	8.72		
ISIK10-3	7.99E-14	8.57E-12	6.22E-14	2.39E-12	236.21	67.52	6.79	0.69	9.46		
ISIK10-4	1.21E-13	1.29E-11	9.39E-14	1.91E-12	202.75	77.41	7.01	0.70	9.52		
ISIK10-5	5.29E-14	4.97E-12	3.61E-14	2.19E-12	193.67	64.81	7.48	0.67	10.68		
ISIK11-1	1.28E-13	1.24E-11	9.03E-14	3.98E-12	249.79	75.61	7.40	0.72	9.94	**10.41**	**0.78**
ISIK11-2	3.83E-14	3.15E-12	2.28E-14	7.82E-13	207.30	71.11	8.92	0.69	12.25		
ISIK11-3	*4.22E-14*	*2.10E-12*	*1.52E-14*	*3.48E-13*	*184.66*	*63.05*	*14.98*	*0.66*	*21.43*		
ISIK11-4	4.92E-14	6.07E-12	4.40E-14	4.84E-13	161.10	61.21	6.16	0.64	9.05		

ISIK11-5	*8.26E-14*	*2.25E-11*	*1.63E-13*	*5.99E-12*	*203.70*	*88.21*	*2.68*	*0.74*	*3.49*		
ISIK34-1	1.91E-13	8.53E-11	6.19E-13	3.06E-12	337.56	108.91	1.72	0.80	2.11	**1.99**	**0.08**
ISIK34-2	6.00E-14	2.69E-11	1.95E-13	8.48E-12	253.41	129.63	1.61	0.81	1.94		
ISIK34-3	3.12E-14	1.70E-11	1.23E-13	1.63E-12	230.78	92.72	1.39	0.75	1.79		
ISIK34-4	1.47E-13	6.10E-11	4.42E-13	1.37E-12	313.12	114.32	1.85	0.80	2.27		
ISIK34-5	1.76E-14	9.06E-12	6.57E-14	2.57E-12	283.05	84.61	1.41	0.75	1.82		
ISIK36-1	3.36E-14	8.34E-12	6.05E-14	1.95E-12	209.05	89.11	2.96	0.74	3.86	**3.50**	**0.25**
ISIK36-2	2.33E-14	7.22E-12	5.24E-14	2.03E-12	352.05	74.77	2.35	0.72	3.14		
ISIK36-3	*1.22E-13*	*7.00E-12*	*5.07E-14*	*5.89E-12*	*247.06*	*87.31*	*11.32*	*0.75*	*14.65*		
ISIK37-1	1.31E-13	2.10E-11	1.52E-13	1.15E-11	334.84	90.01	4.29	0.77	5.45	**3.90**	**0.25**
ISIK37-2	2.79E-14	6.26E-12	4.54E-14	2.95E-12	232.58	101.73	3.11	0.77	3.92		
ISIK37-3	4.00E-14	8.53E-12	6.19E-14	3.68E-12	238.01	74.73	3.30	0.71	4.46		
ISIK37-4	5.57E-14	1.61E-11	1.16E-13	6.70E-12	257.92	87.33	2.45	0.75	3.17		
ISIK37-5	3.80E-14	1.39E-11	1.01E-13	4.55E-12	272.40	90.02	1.96	0.76	2.53		
ISIK38-1	1.40E-13	3.81E-11	2.76E-13	6.73E-12	410.88	118.83	2.73	0.82	3.29	**2.81**	**0.27**
ISIK38-2	3.52E-13	1.01E-10	7.35E-13	1.06E-10	582.81	143.12	2.17	0.85	2.52		
ISIK38-3	6.97E-14	1.99E-11	1.44E-13	5.12E-12	291.40	128.71	2.56	0.82	3.08		
ISIK38-5	2.61E-13	9.62E-11	6.98E-13	2.83E-11	382.81	126.01	1.97	0.82	2.34		
ISIK39-1	1.98E-13	3.91E-11	2.84E-13	2.20E-11	379.19	115.22	3.46	0.81	4.18	**3.29**	**0.25**
ISIK39-2	*2.13E-13*	*1.54E-11*	*1.11E-13*	*1.67E-11*	*254.30*	*90.01*	*8.58*	*0.75*	*11.03*		
ISIK39-3	1.39E-12	3.45E-10	2.50E-12	3.60E-12	262.44	94.53	3.11	0.76	3.93		
ISIK39-4	1.24E-13	3.55E-11	2.57E-13	1.41E-11	378.29	85.53	2.48	0.76	3.17		
ISIK39-5	4.85E-14	2.46E-11	1.78E-13	1.19E-11	200.75	72.12	1.37	0.69	1.89		
ISIK41-1	*2.89E-13*	*4.85E-11*	*3.52E-13*	*6.95E-12*	*295.96*	*98.73*	*4.46*	*0.78*	*5.58*	**2.07**	**0.16**
ISIK41-2	2.15E-13	9.04E-11	6.56E-13	8.41E-12	325.80	108.01	1.80	0.80	2.21		
ISIK41-3	2.11E-13	9.59E-11	6.95E-13	1.13E-11	356.58	118.82	1.66	0.81	2.00		
ISIK41-4	1.58E-13	9.46E-11	6.86E-13	7.82E-12	235.30	99.01	1.27	0.77	1.60		
ISIK41-5	1.98E-13	7.22E-11	5.24E-13	1.73E-11	373.76	104.41	2.02	0.79	2.47		
ISIK42-1	5.93E-14	4.18E-11	3.03E-13	9.13E-13	219.93	76.52	1.09	0.71	1.47	**1.30**	**0.07**
ISIK42-2	*1.18E-13*	*1.63E-12*	*1.18E-14*	*8.17E-14*	*330.32*	*94.52*	*55.12*	*0.77*	*69.67*		
ISIK42-3	3.71E-14	2.86E-11	2.07E-13	2.18E-12	303.37	77.41	0.99	0.73	1.31		
ISIK42-4	1.82E-14	1.66E-11	1.21E-13	2.01E-12	229.87	74.73	0.82	0.71	1.12		
ISIK42-5	*1.02E-17*	*2.29E-11*	*1.66E-13*	*1.15E-12*	*252.49*	*66.61*	*0.00*	*0.69*	*0.00*		
ISIK44-1	5.27E-14	3.27E-11	2.37E-13	3.94E-12	310.41	99.91	1.21	0.78	1.52	**1.45**	**0.19**

ISIK44-2	7.17E-15	8.99E-12	6.52E-14	1.15E-12	227.15	73.82	0.60	0.71	0.82		
ISIK44-3	9.83E-15	6.69E-12	4.85E-14	7.50E-13	238.01	79.21	1.11	0.72	1.49		
ISIK44-4	1.10E-14	9.20E-12	6.67E-14	3.65E-13	221.72	68.41	0.92	0.69	1.28		
ISIK44-5	4.13E-14	2.01E-11	1.46E-13	2.12E-13	212.67	72.91	1.59	0.70	2.16		
ISIK45-1	1.21E-14	4.50E-12	3.26E-14	1.01E-12	168.34	72.01	1.99	0.68	2.75	**1.80**	**0.30**
ISIK45-2	7.79E-15	4.03E-12	2.92E-14	3.01E-12	129.42	68.41	1.28	0.65	1.86		
ISIK45-3	3.77E-14	2.49E-11	1.81E-13	3.71E-12	276.02	106.22	1.13	0.79	1.42		
ISIK45-4	7.93E-15	6.85E-12	4.97E-14	6.90E-13	195.45	76.51	0.88	0.71	1.18		
ISIK45-5	*7.25E-15*	*1.61E-10*	*1.17E-12*	*8.91E-13*	*228.05*	*86.41*	*0.03*	*0.74*	*0.05*		

Ft, is the alpha-ejection correction factor. Numbers in italic indicate outliers that were discarded before mean age calculation. Mean ages are the mean of each selected aliquot and the age error is the standard deviation between selected aliquots divided by the square root of the number of aliquots.

Table 4. Models parameters

Parameter name	Parameter range	Units	Parameter Symbol	Reference
Material Properties				
Thermal conductivity	2.5	W/m/K	k	Whipp et al., 2007
Specific heat capacity	800	J/kg/K	c	Whipp et al., 2007
Crustal density	2700	kg/m^3	ρ_c	
Upper mantle density	3200	kg/m^3	ρ_m	
Thermal diffusivity	35	k□^{2}/□□	α	
Volumetric radiogenic heat production	**0-1.5**	μW/m^3	H	
Radiogenic heat production	**0-20**	°C/Myr	A	
Effective elastic thickness of the India plate	20	km		Berthet et al., 2013 Hammer et al., 2013
Pecube Model Parameters				
Mean annual surface temperature in the foreland	25	°C	T_s	
Atmospheric lapse rate	6	°C km^{-1}	L	Naito et al, 2006
Basal Temperature	750	°C	T_b	Mottram et al., 2014b
India-Eurasia convergence rate	**10-20**	mm/yr	ν□□□□	Mukul et al., 2010 Vernant et al., 2014
Convergence partitioning	**0.6-0.8**	n/a	λ	
Model time step	Optimal	years		
Horizontal node spacing	0.9	km		
Vertical node spacing (0-5km)	0.9	km		
Vertical node spacing (5-15km)	2.7	km		
Vertical node spacing (15-50km)	8.1	km		
Model domain	100x220x50	km		
Fault geometry	**Variable**	km	(X_n, Z_n)	Bhattacharyya and Mitra, 2009 Hauck et al., 1998 Acton et al., 2011

Crustal accretion (south boundary)	**Variable**	km	CA_{dist}
Crustal accretion (north boundary)	**Variable**	km	CA_{prox}
Crustal accretion vertical rate	**Variable**	mm/yr	ν_{CA}

Table 5. Inversion results

Inversion name	**SIK01**	**SIK02**	**SIK03**
Number of models	13314	21020	21020
Best misfit	1.06	0.52	0.54
Tb (°C)	750	750	750
A (°C/Myr)	**19.9** (0:20)	**16.1** (0:20)	**13.5** (0:20)
X_6 (km)	175	175	175
Z_6 (km)	43	43	43
X_5 (km)	140	140	140
Z_5 (km)	31	31	31
X_4 (km)	115	115	115
Z_4 (km)	29	29	29
X_3 (km)	**45** (45:55)	**54.5** (45:55)	**47.1** (45:55)
Z_3 (km)	**10** (10:15)	**13** (10:15)	**13.1** (10:15)
X_2 (km)	**10** (10:20)	**19.8** (10:20)	**14.2** (10:20)
Z_2 (km)	**8.8** (5:10)	**6.5** (5:10)	**6** (5:10)
X_1 (km)	0	0	0
E_1 (km)	0.5	0.5	0.5
Convergence rate (v_{conv}) (mm/yr)	**19.9** (10:20)	**12** (10:20)	**12.2** (10:20)
Time step	1	1	1
Running time (Ma)	12-0	12-0	12-0
Partitioning factor (λ)	**0.6** (0.6:0.8)	**0.6** (0.6:0.8)	**0.6** (0.6:0.8)
Vertical accretion rate (v_{CA}) (mm/yr)	n/a	**2.3** (0:10)	**2.2** (0:10)
Vertical accretion zone south limit (CA_{dist}) (km)	n/a	**25** (15:45)	**22.3** (15:45)
Vertical accretion zone north limit (CA_{prox}) (km)	n/a	**69** (45:70)	**69** (45:70)

Values in brackets indicate the investigated range of the free parameters and the lowest misfit values for each parameter are indicated in bold.

Tectonics

Supporting Information for

Late Neogene tectonically driven crustal exhumation of the Sikkim Himalaya: Insights from inversion of multithermochronologic data

Kyle R. Landry[1], Isabelle Coutand[1], David M. Whipp Jr.[2], Djordje Grujic[1], Jeremy K. Hourigan[3]

[1]Department of Earth Sciences, Dalhousie University, P.O. BOX 15000 Halifax, NS, B3H 4R2, CANADA, [2]Institute of Seismology, Department of Geosciences and Geography, P.O. Box 68 (Gustaf Hällströmin katu 2b), FI-00014 University of Helsinki, FINLAND, [3]Department of Earth and Planetary Sciences, University of California Santa Cruz, 1156 High Street, Santa Cruz, CA 95064, USA.

Contents of this file

Introduction

The supporting informations include (S1) a description of the analytical procedure used for the acquisition of apatite fission track thermochronological data, (S2) a description of the analytical procedure used for the acquisition of zircon (U-Th)/He thermochronological data, (S3) a figure in which thermochronological cooling ages are plotted against elevation, (S4) a figure showing correlation matrices calculated from the Neighbourhood Algorithm, and (S5) is the reference list used in the different sections.

S1 - Analytical procedure of apatite fission-track thermochronology

AFT samples were processed and analysed at Dalhousie University; Apatite aliquots were mounted in araldite epoxy on glass slides, ground and polished to expose internal grain surfaces, then etched for 20 s in 5.5M HNO_3 at 21 °C to reveal spontaneous fission tracks. All mounts were prepared using the external-detector method [*Hurford and Green*, 1983]. Samples and CN_5 glass standards were irradiated with thermal neutrons in the Oregon State University reactor. After irradiation, the low-U muscovite detectors that covered apatite grain mounts and glass dosimeter were etched in 40% HF for 45 min at 21 °C to reveal induced fission tracks. Samples were analysed using a Kinetek computer-controlled stage driven by the FTStage software [*Dumitru*, 1993] attached to a Zeiss Axioplan microscope. Dry counting was done at a magnification of x1000 and between 7 to 30 grains per sample were analysed. Fission track ages were calculated using a weighted mean Zeta calibration factor [*Hurford and Green*, 1983] based on IUGS ages standards (Durango, Fish Canyon and Mount Dromedary apatites) [*Hurford*, 1990; *Miller et al.*, 1985]. Based on 27 analyses, the ζ for the operator (I. Coutand) is 369.8 ± 4.8.

S2 - Analytical procedure of zircon (U-Th)/He thermochronology

Zircon grains were examined using a Zeiss stereoscopic microscope at magnification of x10^6 under both reflected/transmitted and plane- / cross-polarized lights. Grains were selected on the basis of crystal size and geometry with a preference for inclusion-free euhedral grains larger than 65 µm in width [*Reiners*, 2005]. Five acceptable grains were selected for each sample, except for sample ISIK36 in which only three suitable grains were found. A total of 73 aliquots were processed (see Table 3). ^{4}He extraction was completed both at the Dalhousie Noble Gas Extraction Laboratory (ISIK-08-01, 03, 04, 05, 07, 10, 11, 34, 37, 41, 42, 44, 45, along with the first 3 of 5 zircons from samples ISIK-08-38 and 39) and the remaining samples at the Keck Isotope Laboratory at the University of California Santa Cruz (UCSC) (ISIK-08-08, 09, 36, and the remaining 2 grains from samples ISIK-08-38 and 39). Each zircon crystal was photographed and measured for α-ejection correction purposes and was wrapped in Platinum foil to shield the grain from direct laser contact and to prevent shattering and/or uneven heating during ^{4}He extraction. Packages were placed on a planchet within a vacuum-sealed chamber, and heated in sequence at 1300°C for 30 minutes at Dalhousie line and at 1250°C in several 10 minute intervals at UCSC. Meanwhile a pressure line attached to the planchet was voided to a high vacuum (~10^{-8} torr) and then injected with a manometrically calibrated amount of ^{3}He spike (0.1 - 1 pmol). The ^{4}He extracted from the sample was then introduced to the pressure line where it equilibrated with the spike and was introduced into the mass spectrometer for measurement. For each grain, ^{4}He/^{3}He ratio was measured over 30 cycles in order to obtain a mean ratio. The extraction process was then repeated a second time to retrieve any remaining ^{4}He within the grains. If the re-extracted quantity of gas was > 2.5 % of the gas initially obtained, then the procedure was repeated until the amount of gas extracted was < 2.5%. For most samples, a single re-extraction was sufficient. Finally, line blank, cold blank, hot blank and ^{4}He standard measurements were processed between every five extractions. Parent isotopes including ^{238}U, ^{235}U and ^{232}Th were measured at UCSC. Zircons were removed from the Pt foils, rewrapped in niobium tubes, placed into individual teflon tubes and mixed with ~30 mg of spike solution comprising 7.55 ± 0.10 ng/ml ^{236}U and 12.3 ± 0.10 ng/ml ^{229}Th and with a solution comprised of 1:8 ratio of hydrofluoric acid (HF) and nitric acid (HNO_3) to dissolve the grains. The tubes were then inserted into high-pressure digestion vessels (or Parr bombs) which were placed in an oven at ~220°C for about 72 hours to ensure full dissolution. The solution was introduced into a high-resolution (single-collector) Element-2 ICP-MS, which measured the ratios of natural isotopes (^{238}U and ^{232}Th) to spike isotopes (^{236}U and ^{229}Th). Several spiked and acid blanks were analysed concurrently with the samples to test the analytical precision.

S3 - Relationship between cooling ages and elevation

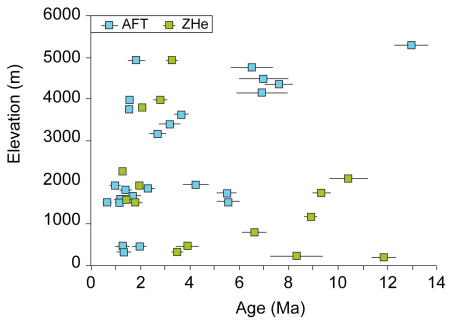

Figure S3. Thermochronologic ages plotted against elevation. Notice the absence of correlation between elevation and both AFT (blue squares) and ZHe (green squares) cooling ages.

S4 - Correlation matrices calculated from the Neighbourhood Algorithm [*Sambridge*, 1999b]

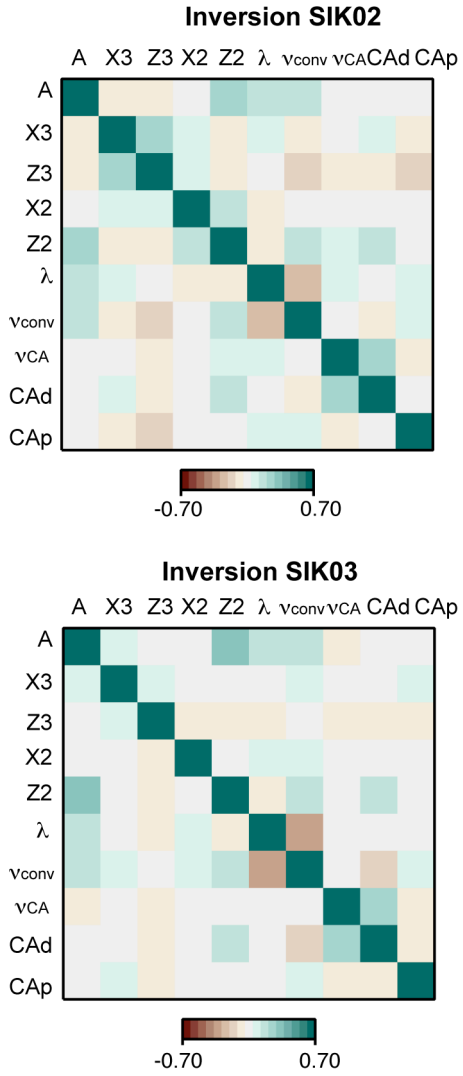

Figure S4. Correlation matrices between the different free parameters calculated for each inversion from the neighborhood algorithm [*Sambridge*, 1999a]. Each raw and column represents a free parameter. Each square represents the correlation (or anti-correlation) between two parameters. The closer the value to -0.7 (0.7), the larger the (anti)correlation. A value equal to 0 indicates the absence of trade-off between the two parameters. Parameters are labelled as in Table 4.

S5 – Reference list

Dumitru, T. A. (1993), A new computer-automated microscope stage system for fission track analysis, *Nuclear Tracks and Radiation Measurements*, *21*, 575-580.

Hurford, A. J. (1990), Standardization of fission-track dating calibration: recommendation by the Fission Track Working Group of the I.U.G.S. Subcommission on geochronology, *Chemical Geology*, *80*, 171-178.

Hurford, A. J., and P. F. Green (1983), The zeta age calibration of fission-track dating, *Isotope Geoscience*, *1*, 285-317.

Miller, D. S., I. R. Duddy, P. F. Green, A. J. Hurford, and C. W. Naeser (1985), Results of interlaboratory comparison of fission-track age standards, *Nuclear Tracks and Radiation Measurements*, *10*, 381-391.

Reiners, P. W. (2005), Zircon (U-Th)/He thermochronometry, *Reviews in Mineralogy and Geochemistry*, *58*(1), 151-179.

Sambridge, M. (1999a), Geophysical inversion with a neighbourhood algorithm -I. Searching a parameter space, *Geophysical Journal International*, *138*, 479-494.

Sambridge, M. (1999b), Geophysical inversion with a neighbourhood algorithm—II. Appraising the ensemble, *138*(3), 727-746.